

An excitable signal integrator couples to an idling cytoskeletal oscillator to drive cell migration

Chuan-Hsiang Huang^{1,3}, Ming Tang^{1,3}, Changji Shi², Pablo A. Iglesias² and Peter N. Devreotes^{1,4}

It is generally believed that cytoskeletal activities drive random cell migration, whereas signal transduction events initiated by receptors regulate the cytoskeleton to guide cells. However, we find that the cytoskeletal network, involving SCAR/WAVE, Arp 2/3 and actin-binding proteins, is capable of generating only rapid oscillations and undulations of the cell boundary. The signal transduction network, comprising multiple pathways that include Ras GTPases, PI(3)K and Rac GTPases, is required to generate the sustained protrusions of migrating cells. The signal transduction network is excitable, exhibiting wave propagation, refractoriness and maximal response to suprathreshold stimuli, even in the absence of the cytoskeleton. We suggest that cell motility results from coupling of 'pacemaker' signal transduction and 'idling motor' cytoskeletal networks, and various guidance cues that modulate the threshold for triggering signal transduction events are integrated to control the mode and direction of migration.

Cells migrate by production of pseudopodia, lamellipodia or other protrusions^{1–5}. It is thought that the morphology and timing of these protrusions derive from regulation of actin polymerization by Rho family GTPases, the SCAR/WAVE complex and other actin-associated proteins^{6–10}, whereas signalling events such as activation of Ras GTPases and phosphatidylinositol-3-OH kinases (PI(3)Ks) triggered by external cues only guide cell migration. However, signalling events also occur at the leading edges of spontaneous protrusions in unstimulated cells^{11,12} and feedback loops involving Ras, PI(3)K, Rac and/or F-actin have been suggested to be involved in cell motility and polarity^{12–14}. Recently, flashes, patches or wave-like propagation of cytoskeletal and signalling activities have been observed at the basal surface of migrating cells or phagocytic cups^{15–25}. These events have been modelled as the behaviour of reaction–diffusion systems, although direct evidence for excitability is lacking, and are presumed to somehow organize the dynamic behaviour of protrusions^{23,24,26–29}. However, it is not clear whether the spontaneous signalling activities are required for motility or how they might coordinate cytoskeletal activities.

RESULTS

To visualize the dynamic behaviour of cytoskeletal and signalling events at the basal surface of migrating cells, we used total internal reflection fluorescence (TIRF) microscopy to examine *Dictyostelium* cells expressing representative biosensors. For cytoskeletal events we used a SCAR/WAVE component HSPC300 (HSPC300) and an actin

polymerization sensor, LimEΔcoil (LimE; ref. 30). For signalling events we used a Ras activation sensor, Raf1-RBD (RBD; ref. 31) and a PIP3 sensor, PH-CRAC (PH; ref. 32). We previously noted that dynamic HSPC300 activities had a finer structure than those of RBD or PH (ref. 24). A more careful analysis revealed closely localized patterns between HSPC300 and LimE and between RBD and PH (correlation coefficients 0.84 ± 0.04 and 0.88 ± 0.04 , respectively (mean \pm s.d., $n = 10$)) but only partial overlap between RBD and LimE (correlation coefficient 0.68 ± 0.04 (mean \pm s.d., $n = 10$)).

To facilitate analysis of the spatiotemporal evolution of these events, we stacked all the frames from a TIRF time-lapse video to create a three-dimensional kymograph, or *t*-stack (Fig. 1a,b and Supplementary Videos 1 and 2 and Fig. 1a for illustration). In this representation, the *z* axis is the time axis of the TIRF video. The *t*-stack can be rotated to view the lateral surface, which represents activity near the edge of the basal surface of the cell (Fig. 1b and Supplementary Video 2). *t*-stacks reveal features of the dynamic activities of biosensors that are not readily apparent by observation of the videos.

The fast oscillatory cytoskeletal network

Unexpectedly, *t*-stacks of cells expressing either HSPC300–GFP or LimE–RFP revealed rapid oscillatory activity at convex, non-expanding points around the perimeter of the basal surface of the cell (Fig. 1b–d). The oscillations had a period of ~ 10 s (Fig. 1c), which was much shorter than the typical interval between pseudopodia. *t*-stack analyses of

¹Department of Cell Biology, Johns Hopkins School of Medicine, Baltimore, Maryland 21205, USA. ²Department of Electrical and Computer Engineering, Johns Hopkins University, Baltimore, Maryland 21218, USA. ³These authors contributed equally to this work.

⁴Correspondence should be addressed to P.N.D. (e-mail: pnd@jhmi.edu)

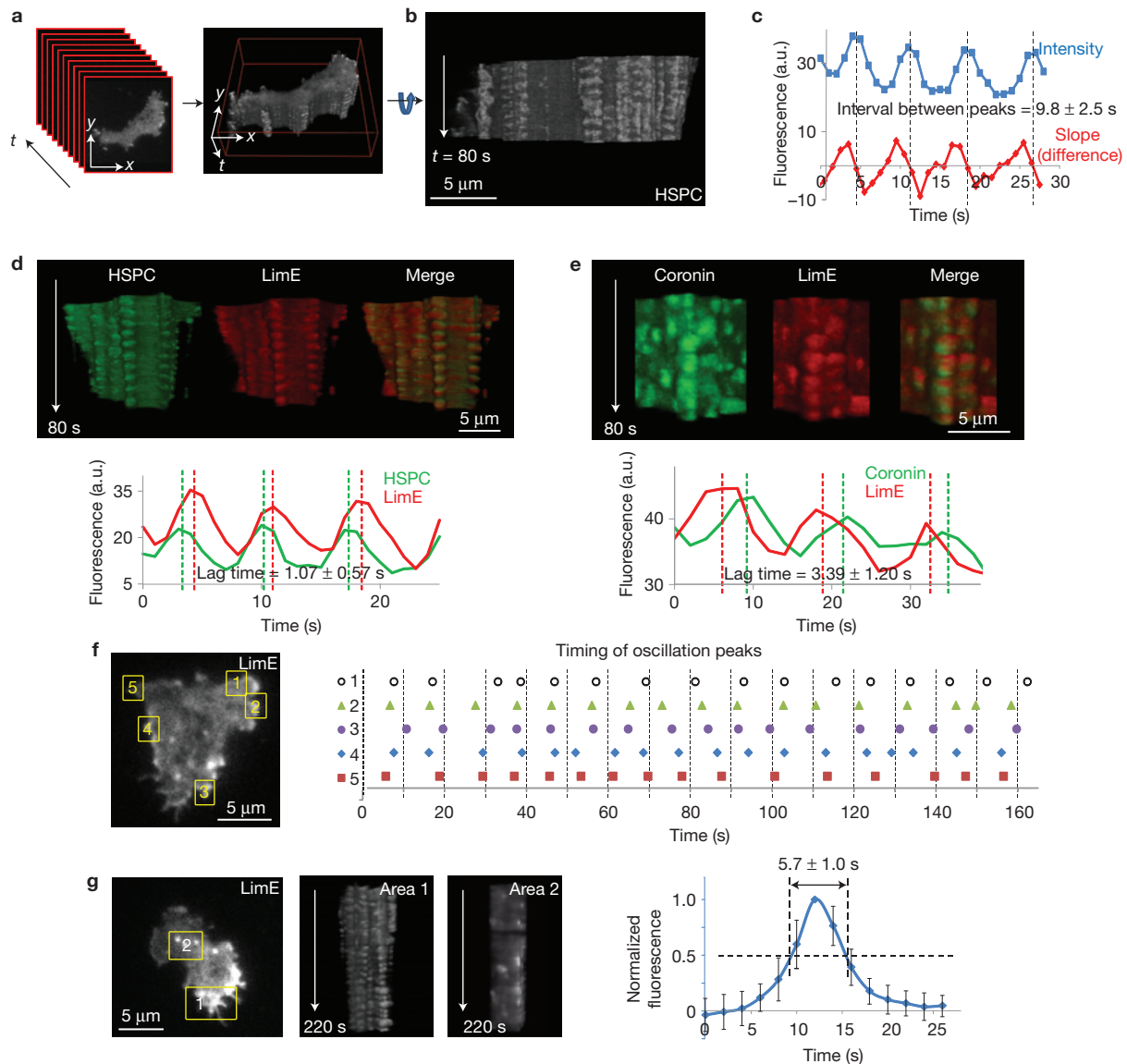


Figure 1 Fast oscillations of the cytoskeletal activities revealed by *t*-stacking. (a,b) A *t*-stack generated by stacking frames of a TIRF video of a cell expressing HSPC300-GFP (Supplementary Video 1). Supplementary Video 2 shows rotation of the *t*-stack along its *t*-axis. (c) Intensity plot (blue) and plot of difference between successive points (red) of an oscillatory region. Peaks of the intensity plot were interpolated from the zero points of the difference plot (dashed lines). The mean ± s.d. of intervals between peaks ($n = 178$ cycles from 16 cells) is shown. (d) *t*-stacks from a cell co-expressing HSPC300-GFP and LimE-RFP (top), and the corresponding intensity plots along an oscillatory region on the periphery (bottom). Dashed lines mark the interpolated peaks. The mean ± s.d. of lags

between the peaks of HSPC300 and LimE intensity ($n = 117$ cycles from 16 cells) is shown. Frame rate: 1 spf. (e) *t*-stacks from a cell co-expressing coronin-GFP and LimE-RFP (top), and the corresponding intensity plots along an oscillatory region on the periphery (bottom). Dashed lines mark the interpolated peaks. The mean ± s.d. of lags between the peaks of coronin and LimE intensity ($n = 256$ cycles from 14 cells) is shown. Frame rate: 2 spf. (f) Timing of peaks of LimE intensity in five oscillatory regions (1–5) within the same cell. (g) *t*-stacks of a peripheral region (area 1) and an internal region (area 2) from a cell expressing LimE. The temporal profile of the internal flashes and the half-maximum width (mean ± s.d., $n = 70$ flashes in 14 cells) is shown on the right.

published videos of the actin crosslinking protein dynacortin³³ and Arp3 (ref. 30) in wild-type cells as well as WASP in *scar*– cells³⁴ also revealed fast oscillations at the basal surface (Supplementary Fig. 1b–d). The oscillations occurred at the front and back of migrating cells, and were often derived from earlier pseudopodia that regressed but remained attached to the substrate (Supplementary Fig. 1b arrowheads). The changes in intensity were not due to displacement of the membrane into the TIRF field because a membrane marker cAR1 did not exhibit oscillations (Supplementary Fig. 1e).

A closer examination of a dual-colour *t*-stack showed that the peaks of HSPC300 preceded those of LimE by ~1 s in the oscillatory cycle (Fig. 1d). In contrast, peaks of coronin, a regulator of actin disassembly³⁵, lagged behind those of LimE by ~3 s (Fig. 1e).

The cytoskeletal activities exhibit a number of features. First, within the same cell, the oscillations at different spots were not in phase with each other, nor did they have identical frequencies (Fig. 1f). Second, oscillations could also be found in cells lacking the G-protein β -subunit, in cells lacking the PIP3 phosphatase PTEN, in cells treated with the

PI(3)K inhibitor LY294002, and in cells expressing constitutively active RasC (Supplementary Fig. 1f–i). However, inhibition of actin polymerization with latrunculin completely eliminated the oscillatory activity of HSPC300 (Supplementary Fig. 1j). These results suggest that these rapid cytoskeletal oscillations do not require signal transduction events but need actin polymerization, which is preceded by the nucleation promoting activity of the SCAR/WAVE complex. Third, *t*-stacks from interior regions of cells showed transient non-oscillatory activities of LimE across the cell bottom (Fig. 1g). These bursts of LimE had a width at half-maximum of ~ 5 s, reminiscent of the activities at the edges. This may reflect some intrinsic kinetics of actin polymerization^{36,37}, although the LimE bursts were not accompanied by HSPC300 recruitment.

The slow excitable signal transduction network

In contrast to the cytoskeletal events, the activities of signal transduction markers, which propagated in expanding waves across the basal surface, were broader and lasted longer (Supplementary Fig. 2a and Video 3). The RBD and PH activities were nearly co-localized, and the *t*-stacks of RBD and PH activities were smooth, indicating the absence of fast oscillations (see below). The progression of a wave is clearly seen by the profiles of temporal changes in intensity at three adjacent points (Supplementary Fig. 2b). The wave velocity in the example shown in Supplementary Fig. 2a–c was $12.8 \mu\text{m min}^{-1}$.

Whereas latrunculin A at $1 \mu\text{M}$ blocked cytoskeletal oscillations, the propagating waves of RBD and PH persisted at $5 \mu\text{M}$ (Fig. 2a). In confocal microscopy, the co-localized RBD and PH activities in latrunculin-treated cells appeared as dynamic patches at the rim of the cell (Fig. 2b). We quantified the patches and found that the latrunculin treatment reduced the frequency of new PH patches (Fig. 2c), suggesting that the cytoskeletal activities promote the initiation of signalling events. The signalling activities presented as propagating waves, as irregular zones lasting between 100 and 150 s, or as oscillations with a period of around 200 s (Supplementary Fig. 2d–h and Videos 4–8).

The propagating waves of RBD and PH suggest that the signal transduction network is excitable. To assess this, we stimulated cells expressing RBD–GFP with increasing concentrations of the chemoattractant cyclic AMP and tracked translocation of RBD–GFP to the membrane. The peak decrease of cytosolic RBD–GFP showed a gradual, dose-dependent change saturating at about 10 nM (Fig. 2d). However, with low doses of chemoattractant, recruitment of RBD–GFP to the membrane occurred in discrete patches, whereas with high doses it occurred around the entire periphery. The intensity of response within a patch was as high as the maximal response (Fig. 2e), indicating that the gradual dose-dependent decrease of the cytosolic signal was due to an increase in the size or number of fully activated patches. As an additional test of excitability, we applied short or long saturating cAMP stimuli to individual cells in the presence of latrunculin. A brief (~ 2 s) stimulus led to a response that peaked at around 8 s and returned to the baseline by 25 s. A longer (20 s) stimulus led to a response with the same rise time, peak and initial decline (Fig. 2f), although there was an additional slowly declining phase corresponding to the start of the secondary responses usually seen during continued stimulation^{38,39}. When two brief stimuli were applied to the same cell, the response to the second stimulus depended on the interval (Fig. 2g). A plot of the recovery of sensitivity indicated an absolute refractory period of ~ 9 s and a relative refractory period with an apparent half time of ~ 7.5 s

(Fig. 2h). The existence of propagating waves, the elicitation of patches of maximal intensity with low-dose stimuli, the ability to induce full responses by short stimuli, and the existence of a refractory period are all hallmarks of excitable systems.

Excitability generally implies that there are positive feedbacks between components. Although PI(3)K is generally considered to be a direct downstream target of Ras GTPases, inhibition of PI(3)Ks was shown to reduce the Ras activity in migrating cells, which was attributed to a feedback loop involving Ras, PI(3)K and F-actin¹². To determine whether the feedback between Ras GTPases and PI(3)Ks can occur independently of the cytoskeleton, we examined the effect of PI(3)K inhibition on Ras activity in the presence of latrunculin. Treatment with LY294002 reduced the number of RBD patches in a dose-dependent manner, with elimination at $10 \mu\text{M}$ (Fig. 2i). Moreover, latrunculin-treated *pten*– cells, which have elevated PIP3, exhibited an increased frequency of new RBD patches when compared with wild-type cells (Fig. 2j). These observations suggest the existence of a positive feedback loop from PIP3 to Ras activity that is independent of cytoskeletal activities.

Rac is a key regulator of the cytoskeleton in migrating cells^{8,40,41} and might be expected to behave like the other cytoskeletal markers. To determine the activation pattern of Rac, we expressed PAK1(GBD)–YFP (ref. 42), which binds specifically to the activated forms of Rac1A and Rac1C. These proteins have been shown to be involved in cell migration⁴³. Surprisingly, the spatiotemporal pattern of PAK1(GBD) recruitment matched that of PH rather than LimE (Fig. 3a,b). Consistently, *t*-stacks of PAK1(GBD) did not exhibit fast oscillations as did HSPC300 and LimE (Fig. 3c). Treatment with LY294002 decreased the frequency of new PAK1(GBD) patches (Fig. 3d).

Coordination of cytoskeletal and signalling networks in protrusions

To understand the roles of cytoskeletal and signalling events in cell migration, we examined the cortical recruitment of co-expressed LimE–RFP and RBD–GFP. As shown in Fig. 4a,b and Supplementary Fig. 3a, RBD and LimE signals were both elevated in large expanding regions (brackets), whereas LimE oscillations unaccompanied by RBD were present in non-expanding regions (vertical rectangles). Closer examination revealed that the LimE oscillations were correlated with the small amplitude undulations of the cell boundary (Fig. 4c). We quantified the relationship between RBD and LimE. First, kymographs of RBD and LimE at the cell perimeter confirmed that both were high in expanding regions and low in non-expanding regions (Fig. 4d). Second, the width of LimE activities in protrusions was significantly larger than that in oscillatory regions (Fig. 4e) and was strongly correlated with the width of RBD activities (Fig. 4f). These observations suggest that signal transduction events drive the expansion of cytoskeletal activities in protrusions.

Although LimE and RBD activities were both elevated in the expanding regions, their localizations were not identical, with LimE restricted to a thin region near the edge and RBD distributed over a substantial area of the protrusion (Supplementary Fig. 3b and Video 9). Moreover, LimE recruitment occurred in bursts, whereas RBD exhibited a smoother change over the entire event (Supplementary Fig. 3c). Similarly to LimE, HSPC300 recruitment also occurred as a series of bursts within large protrusions (Supplementary Fig. 3d,e

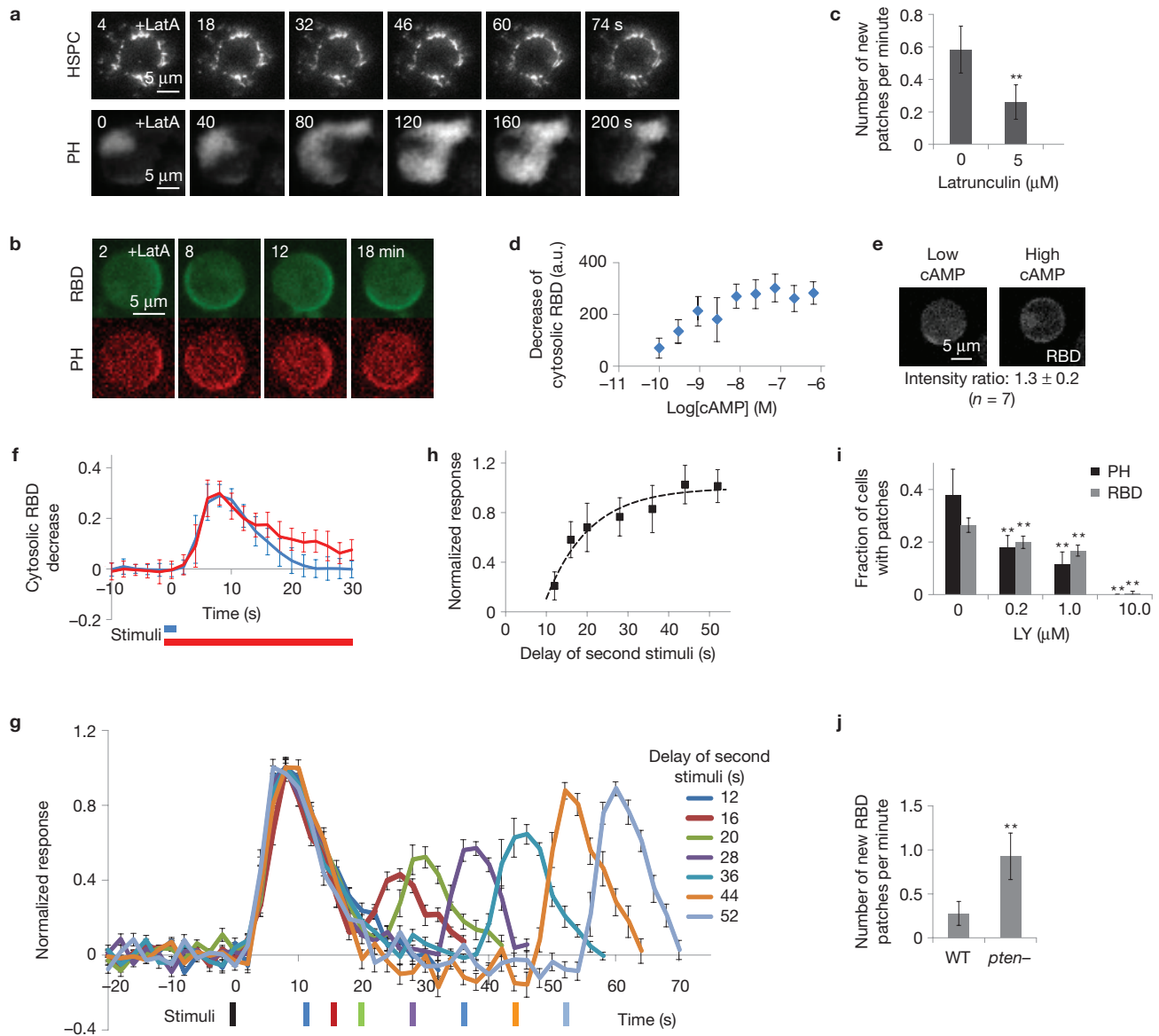


Figure 2 The slow, excitable signalling network. **(a)** Frames from time-lapse TIRF videos of HSPC300–GFP in a cell in $1\mu\text{M}$ latrunculin (upper), and PH–GFP in a cell in $5\mu\text{M}$ latrunculin (lower). **(b)** Frames from a time-lapse video of a latrunculin-treated cell co-expressing RBD–GFP and PH–RFP observed by confocal microscopy. **(c)** The effect of latrunculin on the frequency of new PH–GFP patches (mean \pm s.d., $n = 18$ and 28 cells, $**P < 0.001$, t -test). **(d)** Decrease of cytosolic RBD fluorescence (mean \pm s.d. for $n = 13, 16, 16, 20, 15, 15, 15, 15$ and 7 cells from the lowest to the highest cAMP concentration). **(e)** Example of partial membrane recruitment of RBD–GFP on low-dose (left) and global recruitment on high-dose cAMP stimuli (right). The intensity ratio of patch to global recruitment is shown (mean \pm s.d. for 7 cells). **(f)** Comparison between responses to 2 s (blue) or 20 s (red) stimuli. Responses (mean \pm s.d. for $n = 27$ and 30 cells, respectively) of the cytosolic RBD–GFP decrease were normalized to the pre-stimulus level. **(g)** Responses to two 2 s cAMP

stimuli separated by increasing durations. Black bar: first stimulus. The other bars are colour-coded to show the delay. All values (mean \pm s.e.m., $n = 10, 10, 7, 10, 8, 9$ and 10 cells for 12, 16, 20, 28, 36, 44 and 52 s, respectively) were normalized to the peak of the first response. **(h)** The peak magnitude (mean \pm s.d., $n =$ number of cells as in **g** for each time point) of the second response plotted against the interval between stimuli. The absolute refractory period (8.8 ± 1.1 s) and recovery half-life (7.38 ± 1.74 s) were calculated as described in the Methods. **(i)** Fraction of cells with spontaneous PH and RBD patches in $5\mu\text{M}$ latrunculin and increasing concentrations of LY294002 (LY; mean \pm s.d., $n = 10, 10, 12$ and 15 cells for PH and 40, 40, 50 and 80 cells for RBD for 0, 0.2, 1 and $10\mu\text{M}$ LY294002, respectively). $**P < 0.001$, one-way analysis of variance). **(j)** Frequencies of new RBD patches in wild-type (WT) and *pten*⁻ cells in $5\mu\text{M}$ latrunculin (mean \pm s.d., $n = 10$ cells each; $**P < 0.001$, t -test). **b–j** were obtained by confocal microscopy.

and Video 10). A line kymograph across an expanding pseudopodium revealed that the advancement was broken up into steps, each associated with an increase in HSPC300 (Supplementary Fig. 3f). Thus, when accompanied by signalling events, cytoskeletal activities drive expansions of the cell boundary.

A STEN–CON coupling model of cell migration

Taken together, our findings suggest that the signalling and cytoskeletal events belong to two different networks with distinct characteristics, which we designated as the signal transduction excitable network (STEN) and the cytoskeletal oscillatory network (CON), and that cell

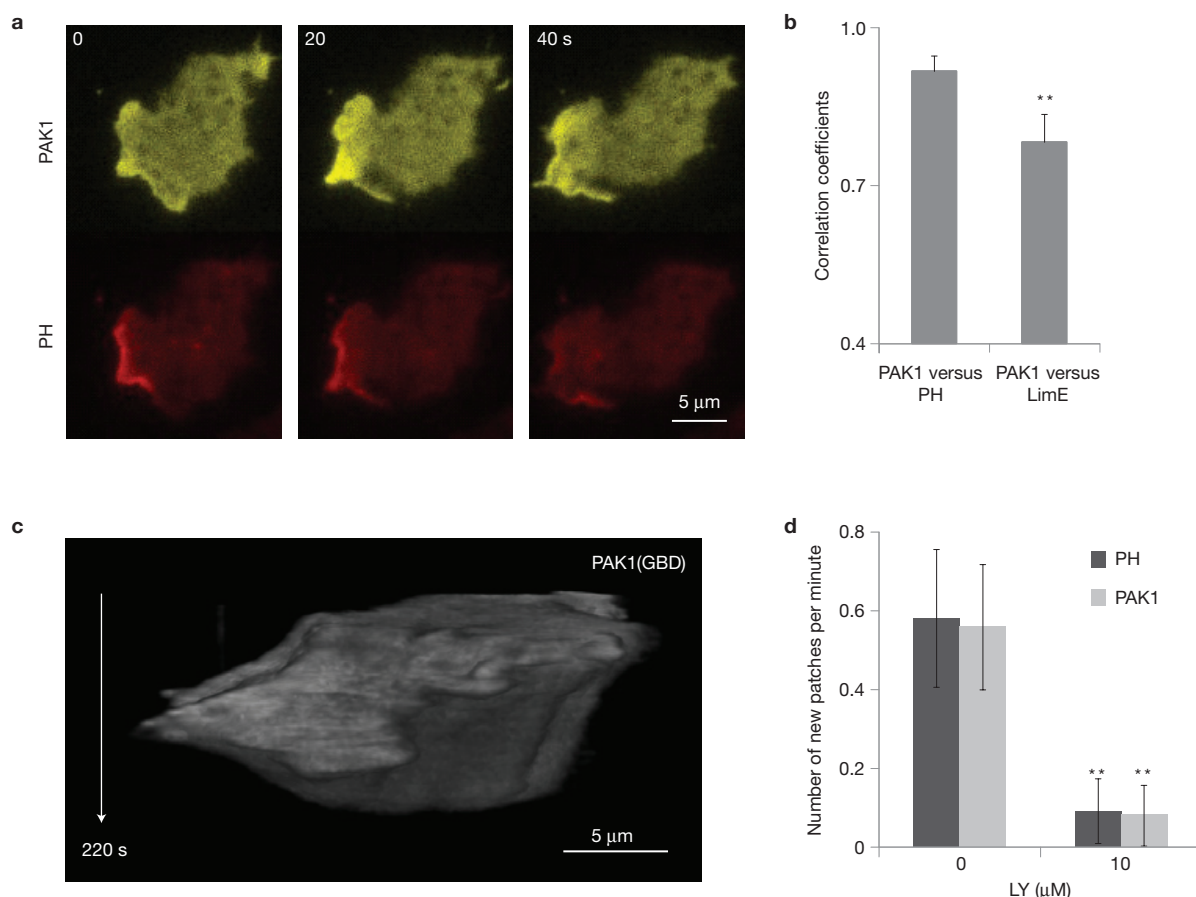


Figure 3 Rac activity correlates with the dynamics of the signalling network. (a) Frames from a time-lapse TIRF video of a cell co-expressing PAK1(GBD)–YFP and PH–RFP. (b) Correlation between pairs of biosensors expressed in the same cells (left: wild-type cells co-expressing PAK1(GBD)–YFP and PH–RFP; right: wild-type cells co-expressing PAK1(GBD)–YFP and LimE–RFP; $n = 10$

cells each, grey bars: mean, error bars: s.d., $**P < 0.001$, t -test). (c) k -stack of a cell expressing the Rac biosensor PAK1(GBD)–YFP showing the absence of fast oscillations. (d) Effect of LY294002 (LY) treatment on the frequency of new patches in cells expressing PAK1(GBD)–YFP and PH–RFP observed by confocal microscopy (mean \pm s.d., $n = 10$ cells each; $**P < 0.001$, t -test).

migration depends on STEN–CON coupling. In this coupling model for cell migration, shown schematically in Fig. 5a, the CON provides the ‘idling’ motor force, which by itself drives only small-amplitude undulations. In large protrusions, the CON is engaged by the activity of the STEN, which acts as the ‘pacemaker’ for cell migration. As a wave of signal transduction activity propagates, it prevents the retraction of expanded areas during the down phase of the cytoskeletal oscillation or completely shifts existing or newly initiated cytoskeletal activities beyond the oscillatory mode to a continuously active state. In either case, the coupling of STEN and CON leads to a widening protrusion. The STEN will fire when the threshold is crossed, whether owing to internal noise or feedback from the CON. The STEN can also be modulated by a variety of external stimuli and perturbations (see Discussion).

Figure 5b summarizes our present working model of the links between components of the STEN and the CON. The STEN is represented by Ras GTPases and PI(3)Ks and feedbacks between them. Rac GTPases are considered part of the STEN because the spatiotemporal patterns of activity of our biosensor match those of the STEN rather than the CON. The CON consists of SCAR/WAVE, Arp2/3, F-actin (represented by LimE and dynacortin) and coronin, which all show rapid oscillations. The temporal relationship and the fact

that it is involved in actin depolymerization suggest that coronin may be part of a negative feedback loop in the CON. The link from the STEN to the CON is indicated by an arrow connecting Rac to SCAR/WAVE based on literature^{44,45} (see Discussion). The link from the CON to the STEN is based on our observation and a recent report⁴⁶ that latrunculin reduces the probability of the STEN activation.

To test the feasibility of using these coupled networks to describe cell migration, we carried out computer simulations based on the scheme shown in Fig. 5c (see Methods for details). The scheme consists of slow and fast systems of the activator–inhibitor class^{28,47}. The slow system was set as an excitable network whereas the fast system was set as a stochastic, bi-stable oscillator (Supplementary Fig. 4). Coupling between the two systems is bidirectional such that perturbations in either system influence the activity of the other. The slow and fast systems in the scheme correspond to the STEN and the CON, respectively. In simulations we recapitulated the oscillations of the CON in the absence of activity of the STEN (region 1 in Fig. 5d,e), and the broadening of the CON activities accompanied by the activation of the STEN while preserving the characteristic time constants (region 2 in Fig. 5d,e). We further used the activity of the coupled systems to drive the movement of the boundary of a cell and simulated realistic behaviour (Supplementary Video 11).

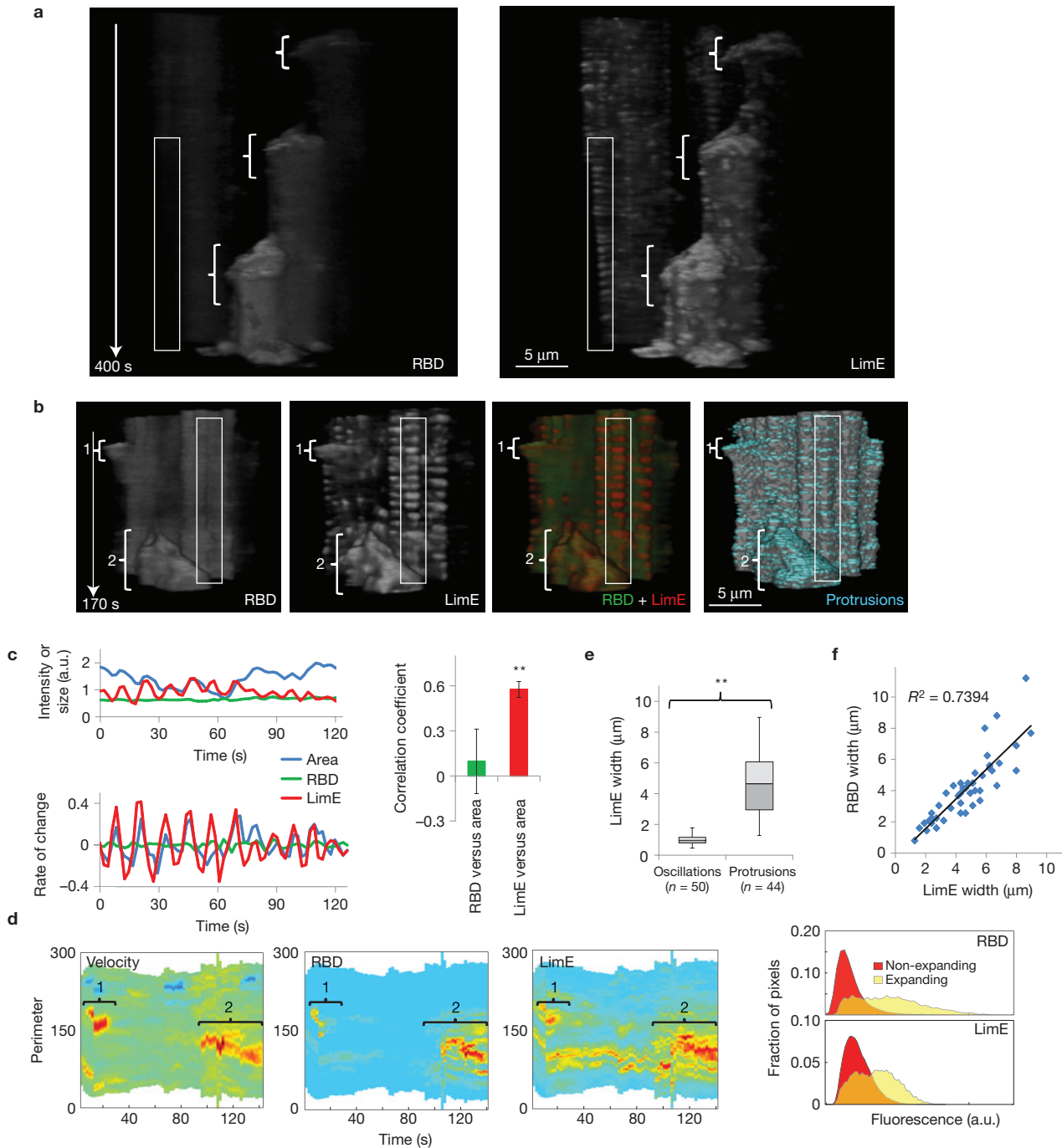


Figure 4 Coupling of signal transduction and cytoskeletal networks in protrusions. **(a)** *t*-stacks from two cells co-expressing RBD-GFP (left) and LimE-RFP (right). In each panel, the cell on the right extends three large protrusions (brackets) during the imaging period. The outlined area on the non-extending cell on the left shows oscillations in LimE-RFP without apparent oscillations in RBD-GFP. **(b)** *t*-stacks from another cell co-expressing RBD-GFP and LimE-RFP and used for quantitative analysis. The brackets point to two protrusions (the smaller labelled 1, the larger labelled 2) with high RBD and LimE, which appear yellow in the merged *t*-stack (third panel). The 'protrusion' *t*-stack shows regions of cell boundary increases in blue (fourth panel). In contrast, fast LimE oscillations accompanying cell boundary undulations appear red (rectangle in third panel). Note that weak oscillations in the RBD *t*-stacks in **a,b** reflect changes in the boundary that delineates cytosolic RBD rather than RBD intensity on the cortex. **(c)** Intensities of RBD-GFP and LimE-RFP plotted along with the cellular area in a region with LimE oscillation (left upper), as well as the

rate of change calculated from the difference between values in successive frames (left lower). Rate of change of LimE-RFP shows significantly higher correlation with that of cellular area compared with RBD-GFP (right; $n = 6$ regions from 2 cells; error bars: s.d.; $**P < 0.001$, *t*-test). **(d)** Kymographs of velocity, RBD and LimE around the boundary of the cell in **b** with fast oscillations/undulations filtered out (see Methods). Brackets numbered 1 and 2 correspond to the protrusions in **b**. The histogram (right) shows the intensity distribution of pixels in expanding regions versus non-expanding regions. Similar analyses carried out in 6 cells yielded a mean \pm s.d. right shift of 1.44 ± 0.16 ($P = 0.00075$) for RBD and 1.98 ± 0.41 ($P = 0.0015$, *t*-test) for LimE. **(e)** Box-and-whisker plot comparison of widths of LimE fluorescence in oscillatory regions and expanding protrusions (boxes: first, second and third quartiles; whisker ends: minimum and maximum). The mean \pm s.d. for oscillatory and expanding regions were $0.98 \pm 0.30 \mu$ m ($n = 50$ patches) and $4.69 \pm 1.92 \mu$ m ($n = 44$ patches; $**P < 0.001$, *t*-test). **(f)** Correlation between LimE and RBD widths in expanding pseudopods.

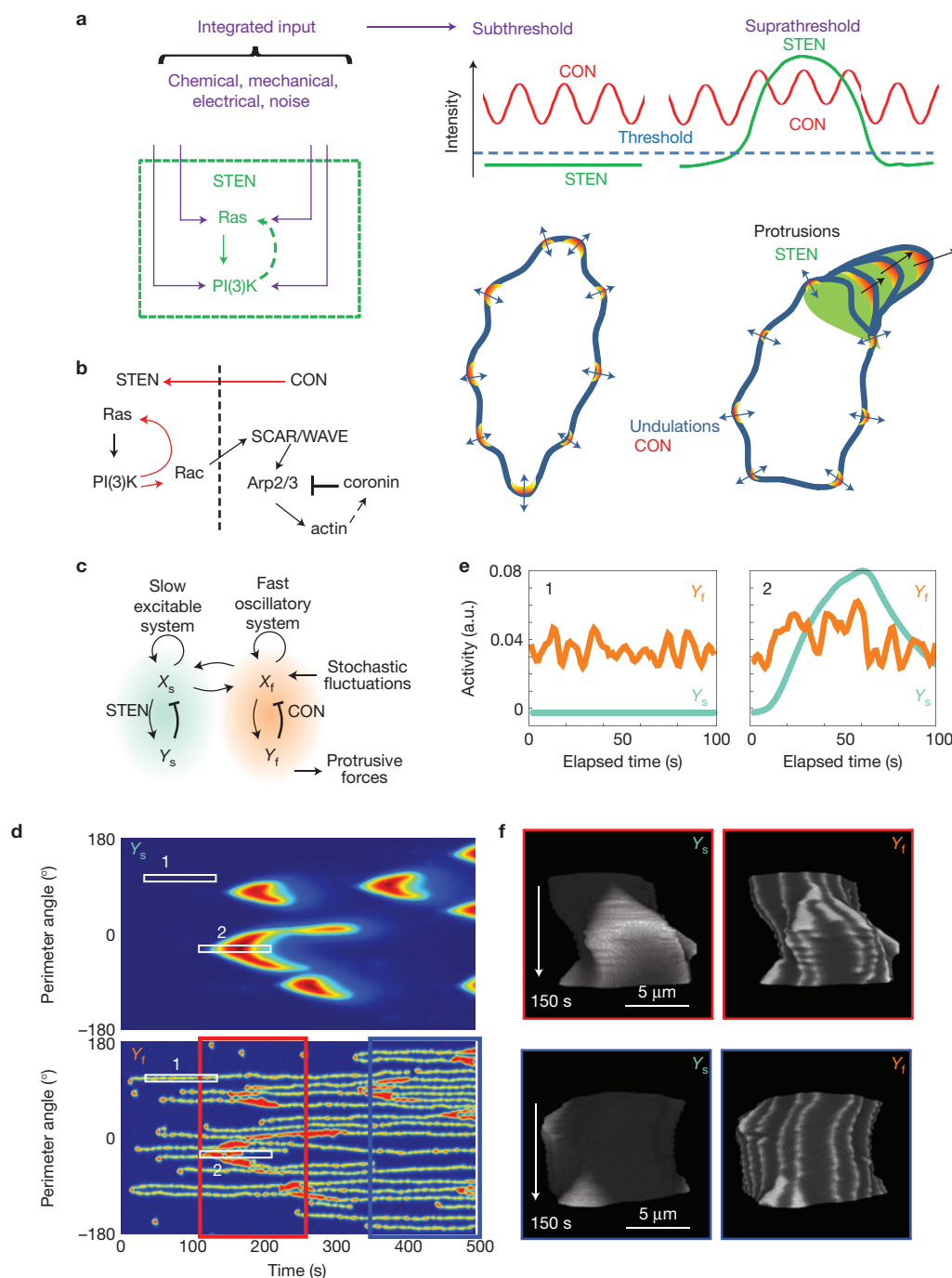


Figure 5 The STEN–CON coupling model and computer simulation. **(a)** In the STEN–CON coupling model, inputs from various sources enter STEN at different points. When the integrated input reaches a threshold level, STEN becomes fully activated and by coupling to CON causes large protrusions. Without STEN activation, the cytoskeletal oscillations cause only small-amplitude undulations of the cell boundary. (Note that the stochastic LimE flashes, similar to those reported previously³⁷, were not accompanied by HSPC300 recruitment and were not considered part of the CON in our definition, despite a similar lifetime of activities as discussed in the main text.) **(b)** Schematic of the links between components of the STEN and CON. Red arrows highlight the links demonstrated in this study. **(c)** The

behaviours of the STEN and the CON were modelled using reaction–diffusion equations describing coupled slow (X_s , Y_s) and fast (X_f , Y_f) activator–inhibitor systems solved in one dimension around a circle (see Methods for details). **(d)** Kymograph describing the activities of the slow (Y_s) and fast (Y_f) systems around the perimeter of the circle using a jet colour map. **(e)** Intensity plots of the slow and fast systems corresponding to rectangles 1 and 2 in **d**. **(f)** The activities of the slow and fast systems were used to control the boundary of a hypothetical cell (Supplementary Video 11). t -stacks of the activities of Y_s and Y_f on the boundary of the hypothetical cell with a grey colour map corresponding to the period from 100 to 250 s (red rectangle) and 350 to 500 s (blue rectangle) in **d** are shown.

Using the boundary to represent the edge of the basal cellular surface we produced t -stacks resembling those derived from TIRF videos of real cells (Fig. 5f).

Predictions of the STEN–CON coupling model

According to the STEN–CON coupling model, blocking activity of the STEN should prevent cells from generating large protrusions

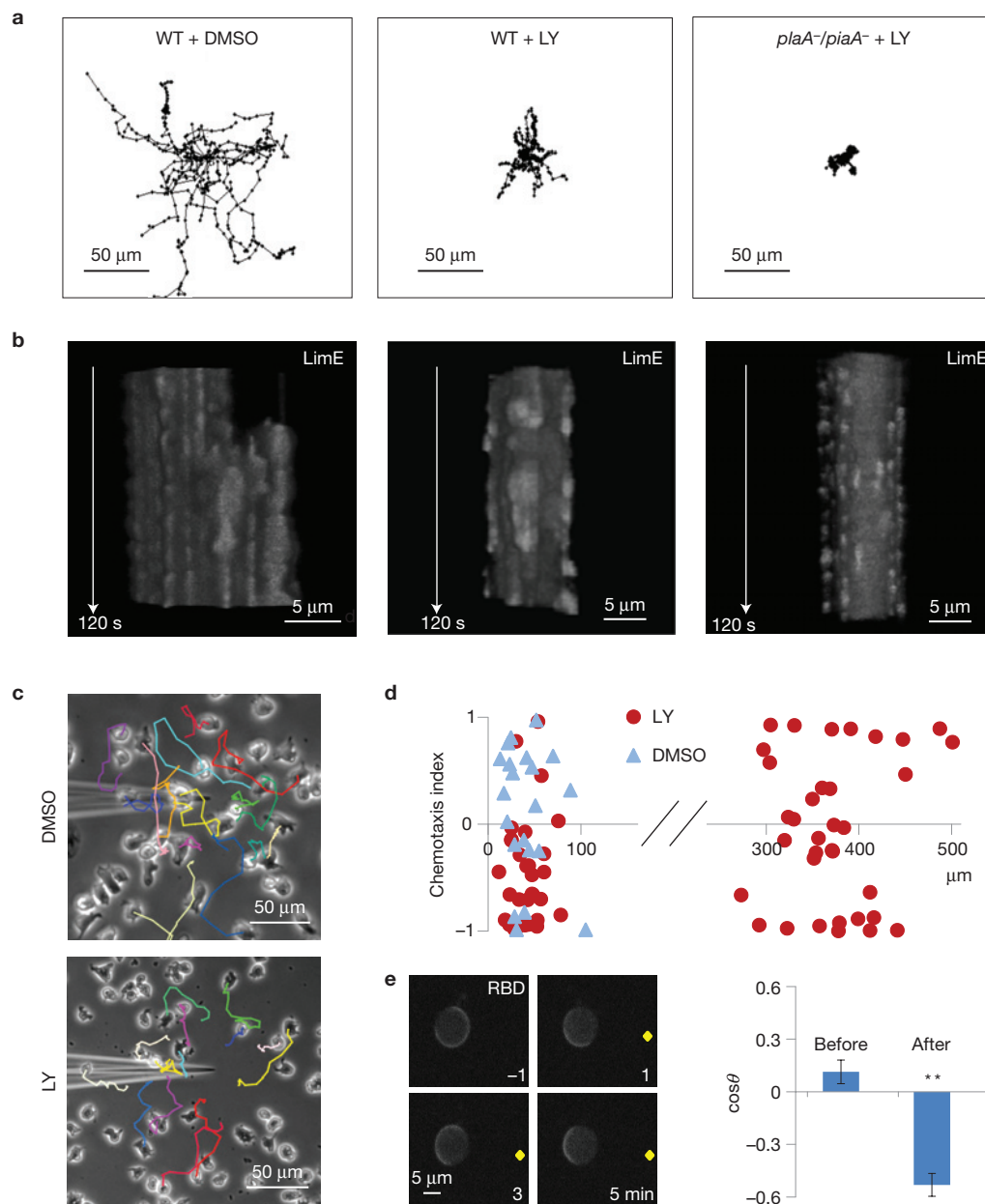


Figure 6 Predictions of STEN-CON coupling for cell migration. **(a)** Centroid tracks of wild-type (WT) cells treated with DMSO (left) or LY294002 (LY; middle), as well as *plaA*⁻/*piaA*⁻ cells treated with LY294002 (right). Duration of tracks: 60 min. **(b)** *t*-stacks of LimE expressed in cells corresponding to those in **a**. **(c)** The centroid tracks of cells in the vicinity of the micropipette filled with 0.4% DMSO (top) or 0.4% DMSO plus 200 μ M LY294002 (bottom) are overlaid on the final image of a 20 min video. **(d)** Quantification of **c** showing the chemotaxis index of cells in a gradient of LY294002 (red circles) or DMSO (blue triangles) versus the distance from the tip of the micropipette. The chemotaxis indices for cells

within 100 μ m from the tip of the LY294002- or DMSO-filled micropipette were -0.48 ± 0.09 (mean \pm s.e.m., $n = 32$ cells) or 0.10 ± 0.14 (mean \pm s.e.m. $n = 21$ cells; $p = 0.00047$, *t*-test). The chemotaxis index for cells between 300 and 400 μ m from the tip of the LY294002-filled micropipette was -0.07 ± 0.12 (mean \pm s.e.m. $n = 30$ cells). **(e)** RBD responses to a gradient generated by a micropipette (tip indicated by yellow dot) filled with 200 μ M LY294002 (left). Cosine angles of the direction of patches before and after placement of micropipette is shown on the right (mean \pm s.e.m.; $n = 138$ and 99 frames from 5 cells, $**P < 0.001$, *t*-test).

and moving substantially but it should not interfere with the CON-driven surface undulations. To test this, we treated wild-type cells with the PI(3)K inhibitor LY294002. These cells showed diminished spontaneous migration (Fig. 6a). However, the defect faded during prolonged treatment, possibly owing to compensation in the network^{38,48}. For this reason we simultaneously blocked the PLA2, TORC2 and PI(3)K pathways by treating *plaA*⁻/*piaA*⁻ cells with

LY294002. These cells showed minimal migration (Fig. 6a), with a net speed, motility speed and persistence of only 5, 24 and 21%, respectively, of those of wild-type cells. Washout of LY294002 restored the motility to that of *plaA*⁻/*piaA*⁻ cells (Supplementary Fig. 5 and Table 2). The frequency of protrusions was 1.35 ± 0.48 ($n = 17$ cells), 0.36 ± 0.23 ($n = 11$ cells) and 0.02 ± 0.04 ($n = 13$ cells) per minute for wild-type cells, LY294002-treated wild-type cells and LY294002-treated

plA-/-piaA- cells, respectively. Importantly, although the non-motile cells lacked large patches of LimE activity and protrusions, they still had the fast oscillations and peripheral undulations (Fig. 6b). These results suggest that STEN activity is required to generate pseudopodia for cell motility but is not essential for the CON-induced surface undulations.

A further prediction of the STEN–CON coupling model is that preferential inhibition of STEN activity on one side of the cell should cause the cell to migrate in the opposite direction. To test this idea, we used a micropipette filled with LY294002 to generate a gradient of PI(3)K inhibition. On introduction of the micropipette, cells closest to the tip rounded up and then migrated away from the tip (Fig. 6c). Cells that were initially heading towards the micropipette were deflected away as they approached. The range of repulsion was limited to $\sim 100\ \mu\text{m}$ from the tip of the micropipette; cells farther from the micropipette were unaffected (Fig. 6d). Cells were not repelled by a micropipette filled with a control concentration of dimethylsulphoxide (DMSO). To demonstrate that the chemorepulsion was due to differential effects on STEN activity we observed spontaneous RBD activity in cells immobilized with latrunculin. Application of the gradient of LY294002 caused initially randomly distributed RBD patches to localize away from the tip of the micropipette (Fig. 6e).

DISCUSSION

The STEN–CON coupling model provides a framework for understanding cell migration. The ‘idling’ activity of the CON provides the force, but it is the ‘pacemaker’ activity of the STEN that determines the timing and size of protrusions in migrating cells. This mechanism has important implications. First, it suggests that activation of the STEN by stochastic noise underlies random cell motility and a cue that affects the threshold for excitation differently on opposite sides of a cell would be expected to guide cell migration. For example, inhibitors of PI(3)K can act as chemorepellents (Fig. 6c–e). As a slight increase in threshold could greatly reduce noise-triggered excitation on one side of the cell, the mechanism could account for the ultrasensitivity of chemotaxing cells. Second, there can be multiple entry points into the STEN. For example, perturbations of the level of PIP3 (Fig. 2i,j) and the activity of Ras (refs 49,50) or Rac (refs 51,52) modulate the frequency of STEN activation. Therefore, external cues that might enter the network through different components can have the same effects on overall activity. Third, we speculate that perturbations and inputs from various guidance cues such as chemical gradients, shear flow⁵³ and electric fields⁵⁴ are integrated in the STEN, where the decision to make a protrusion is based on whether a threshold for triggering the network is reached. We have observed that the effects of simultaneously altering PIP3 levels and cytoskeletal activities are additive (Fig. 2c,i,j). In the future, additional experiments using multiple cues and perturbations can be designed to further test the role of the STEN as an integrator.

The STEN–CON coupling model may explain an array of observations in the literature. First, in mesenchymal cells, small pilot protrusions are reinforced by subsequent PIP3 accumulation⁵⁵, suggesting that the coupled networks we describe may also underlie the migration of fibroblasts and other cells. Second, cells led to migrate by synthetic activation of Rac produce PIP3 at the leading edges, but Rac activation in the absence of PIP3 causes only ruffling^{13,52}, consistent with our conclusion that the STEN is required for large protrusions and migration. Third, a recent study showing damped oscillations of total

actin following a short pulse of chemoattractant⁵⁶ might be explained by transient synchronization of the CON at different points around the periphery of the basal cell surface.

Our work raises several questions to be addressed in future studies. First, the negative feedback that causes the refractory period and is required for the excitability of the STEN is not known. Cells lacking myosin seem to have extended activation of Ras (ref. 57), and a negative feedback involving RasGEF, TORC2 and PKBs has been described⁵⁸. The role of these components can be tested by measuring the effects of their levels on parameters of excitability such as the threshold and refractory period. Second, the mechanism of the coupling between the two networks requires further investigation. We speculated that Rac GTPases are involved in coupling because activation of Rac 1A/1C exhibited the kinetics of the STEN and, as might be expected from observations that Rac GTPases directly link to the SCAR/WAVE complex^{44,45}, constitutively active Rac 1A causes excessive cytoskeletal activity in these cells⁴³. The mechanism of the reverse coupling, from CON to STEN, remains to be determined. Third, it is not clear whether coordination of CON activity is the sole reason that STEN activity is required for motility. In addition to actin polymerization, successful cell migration requires attachment of the protrusions to the substrate and myosin-based contractile events. STEN activity may also control these aspects of migration. □

METHODS

Methods and any associated references are available in the [online version of the paper](#).

Note: Supplementary Information is available in the online version of the paper

ACKNOWLEDGEMENTS

The authors would like to thank M. Amzel, D. Montell, M. Iijima, T. Inoue and members of the Devreotes and Iglesias laboratories for helpful suggestions, B. Diplas for generating cell centroid tracks, P. Van Haastert for the RBD–GFP construct, R. Insall (The Beatson Institute, UK) for the HSPC300–GFP construct, G. Gerisch (Max Planck Institute for Biochemistry, Germany) for the LimE–RFP construct, and D. Robinson (Johns Hopkins University, USA) for coronin–GFP and the original video of dynacortin-expressing cells. We are grateful to V. Filic and I. Weber (Ruder Boskovic Institute, Croatia) for sharing the PAK(GBD)–YFP biosensor for Rac activity. This work was supported in part by grants from the National Institutes of Health, GM28007 (to P.N.D.), GM34933 (to P.N.D.) and GM71920 (to P.A.I.), and a H. L. Plotnick Fellowship from the Damon Runyon Cancer Research Foundation, DRG2019-09 (to C.H.H.).

AUTHOR CONTRIBUTIONS

C.H.H. and M.T. performed the experiments. C.S. and P.A.I. carried out computer simulations. All authors analysed the data and wrote the manuscript. P.N.D. supervised the study.

COMPETING FINANCIAL INTERESTS

The authors declare no competing financial interests.

Published online at www.nature.com/doifinder/10.1038/ncb2859

Reprints and permissions information is available online at www.nature.com/reprints

1. Ridley, A. J. *et al.* Cell migration: integrating signals from front to back. *Science* **302**, 1704–1709 (2003).
2. Bosgraaf, L. & Van Haastert, P. J. The ordered extension of pseudopodia by amoeboid cells in the absence of external cues. *PLoS ONE* **4**, e5253 (2009).
3. Tranquillo, R. T., Lauffenburger, D. A. & Zigmond, S. H. A stochastic model for leukocyte random motility and chemotaxis based on receptor binding fluctuations. *J. Cell Biol.* **106**, 303–309 (1988).
4. Arriuerlou, C. & Meyer, T. A local coupling model and compass parameter for eukaryotic chemotaxis. *Dev. Cell* **8**, 215–227 (2005).
5. Welf, E. S. & Haugh, J. M. Signaling pathways that control cell migration: models and analysis. *Wires Syst. Biol. Med.* **3**, 231–240 (2011).

6. Pollard, T. D. & Borisy, G. G. Cellular motility driven by assembly and disassembly of actin filaments. *Cell* **112**, 453–465 (2003).
7. Hall, A. Rho GTPases and the control of cell behaviour. *Biochem. Soc. Trans.* **33**, 891–895 (2005).
8. Ridley, A. J. Rho GTPases and actin dynamics in membrane protrusions and vesicle trafficking. *Trends Cell Biol.* **16**, 522–529 (2006).
9. Machacek, M. *et al.* Coordination of Rho GTPase activities during cell protrusion. *Nature* **461**, 99–103 (2009).
10. Welch, C. M., Elliott, H., Danuser, G. & Hahn, K. M. Imaging the coordination of multiple signalling activities in living cells. *Nat. Rev. Mol. Cell Biol.* **12**, 749–756 (2011).
11. Cain, R. J. & Ridley, A. J. Phosphoinositide 3-kinases in cell migration. *Biol. Cell* **101**, 13–29 (2009).
12. Sasaki, A. T. *et al.* G protein-independent Ras/PI3K/F-actin circuit regulates basic cell motility. *J. Cell Biol.* **178**, 185–191 (2007).
13. Inoue, T. & Meyer, T. Synthetic activation of endogenous PI3K and Rac identifies an AND-gate switch for cell polarization and migration. *PLoS ONE* **3**, e3068 (2008).
14. Weiner, O. D. *et al.* A PtdInsP(3)- and Rho GTPase-mediated positive feedback loop regulates neutrophil polarity. *Nat. Cell Biol.* **4**, 509–513 (2002).
15. Asano, Y., Nagasaki, A. & Uyeda, T. Q. Correlated waves of actin filaments and PIP3 in *Dictyostelium* cells. *Cell Motil. Cytoskeleton* **65**, 923–934 (2008).
16. Bretschneider, T. *et al.* The three-dimensional dynamics of actin waves, a model of cytoskeletal self-organization. *Biophys. J.* **96**, 2888–2900 (2009).
17. Case, L. B. & Waterman, C. M. Adhesive F-actin waves: a novel integrin-mediated adhesion complex coupled to ventral actin polymerization. *PLoS ONE* **6**, e26631 (2011).
18. Gerisch, G. Self-organizing actin waves that simulate phagocytic cup structures. *PMC Biophys.* **3**, 7 (2010).
19. Gerisch, G. *et al.* Self-organizing actin waves as planar phagocytic cup structures. *Cell Adhes. Migr.* **3**, 373–382 (2009).
20. Gerisch, G. *et al.* Mobile actin clusters and traveling waves in cells recovering from actin depolymerization. *Biophys. J.* **87**, 3493–3503 (2004).
21. Vicker, M. G. F-actin assembly in *Dictyostelium* cell locomotion and shape oscillations propagates as a self-organized reaction-diffusion wave. *FEBS Lett.* **510**, 5–9 (2002).
22. Vicker, M. G. Eukaryotic cell locomotion depends on the propagation of self-organized reaction-diffusion waves and oscillations of actin filament assembly. *Exp. Cell Res.* **275**, 54–66 (2002).
23. Weiner, O. D., Marganski, W. A., Wu, L. F., Altschuler, S. J. & Kirschner, M. W. An actin-based wave generator organizes cell motility. *PLoS Biol.* **5**, e221 (2007).
24. Xiong, Y., Huang, C. H., Iglesias, P. A. & Devreotes, P. N. Cells navigate with a local-excitation, global-inhibition-biased excitable network. *Proc. Natl Acad. Sci. USA* **107**, 17079–17086 (2010).
25. Arai, Y. *et al.* Self-organization of the phosphatidylinositol lipids signaling system for random cell migration. *Proc. Natl Acad. Sci. USA* **107**, 12399–12404 (2010).
26. Hecht, I., Kessler, D. A. & Levine, H. Transient localized patterns in noise-driven reaction-diffusion systems. *Phys. Rev. Lett.* **104**, 158301 (2010).
27. Vicker, M. G. Reaction-diffusion waves of actin filament polymerization/depolymerization in *Dictyostelium* pseudopodium extension and cell locomotion. *Biophys. Chem.* **84**, 87–98 (2000).
28. Meinhardt, H. Orientation of chemotactic cells and growth cones: models and mechanisms. *J. Cell Sci.* **112**, 2867–2874 (1999).
29. Hecht, I. *et al.* Activated membrane patches guide chemotactic cell motility. *PLoS Comput. Biol.* **7**, e1002044 (2011).
30. Bretschneider, T. *et al.* Dynamic actin patterns and Arp2/3 assembly at the substrate-attached surface of motile cells. *Curr. Biol.* **14**, 1–10 (2004).
31. Kae, H., Lim, C. J., Spiegelman, G. B. & Weeks, G. Chemoattractant-induced Ras activation during *Dictyostelium* aggregation. *EMBO Rep.* **5**, 602–606 (2004).
32. Parent, C. A., Blacklock, B. J., Froehlich, W. M., Murphy, D. B. & Devreotes, P. N. G protein signaling events are activated at the leading edge of chemotactic cells. *Cell* **95**, 81–91 (1998).
33. Kabacoff, C. *et al.* Dynacortin facilitates polarization of chemotaxing cells. *BMC Biol.* **5**, 53 (2007).
34. Veltman, D. M., King, J. S., Machesky, L. M. & Insall, R. H. SCAR knockouts in *Dictyostelium*: WASP assumes SCAR's position and upstream regulators in pseudopods. *J. Cell Biol.* **198**, 501–508 (2012).
35. Uetrecht, A. C. & Bear, J. E. Coronins: the return of the crown. *Trends Cell Biol.* **16**, 421–426 (2006).
36. Sirotkin, V., Berro, J., Macmillan, K., Zhao, L. & Pollard, T. D. Quantitative analysis of the mechanism of endocytic actin patch assembly and disassembly in fission yeast. *Mol. Biol. Cell* **21**, 2894–2904 (2010).
37. Uchida, K. S. & Yumura, S. Dynamics of novel feet of *Dictyostelium* cells during migration. *J. Cell Sci.* **117**, 1443–1455 (2004).
38. Chen, L. *et al.* Two phases of actin polymerization display different dependencies on PI(3,4,5)P3 accumulation and have unique roles during chemotaxis. *Mol. Biol. Cell* **14**, 5028–5037 (2003).
39. Postma, M. *et al.* Uniform cAMP stimulation of *Dictyostelium* cells induces localized patches of signal transduction and pseudopodia. *Mol. Biol. Cell* **14**, 5019–5027 (2003).
40. Ridley, A. J., Paterson, H. F., Johnston, C. L., Diekmann, D. & Hall, A. The small GTP-binding protein rac regulates growth factor-induced membrane ruffling. *Cell* **70**, 401–410 (1992).
41. Jaffe, A. B. & Hall, A. Rho GTPases: biochemistry and biology. *Annu. Rev. Cell Dev. Biol.* **21**, 247–269 (2005).
42. Filic, V., Marinovic, M., Faix, J. & Weber, I. A dual role for Rac1 GTPases in the regulation of cell motility. *J. Cell Sci.* **125**, 387–398 (2012).
43. Dumontier, M., Hocht, P., Mintert, U. & Faix, J. Rac1 GTPases control filopodia formation, cell motility, endocytosis, cytokinesis and development in *Dictyostelium*. *J. Cell Sci.* **113**, 2253–2265 (2000).
44. Eden, S., Rohatgi, R., Podtelejnikov, A. V., Mann, M. & Kirschner, M. W. Mechanism of regulation of WAVE1-induced actin nucleation by Rac1 and Nck. *Nature* **418**, 790–793 (2002).
45. Kitamura, Y. *et al.* Interaction of Nck-associated protein 1 with activated GTP-binding protein Rac. *Biochem. J.* **322**, 873–878 (1997).
46. Taniguchi, D. *et al.* Phase geometries of two-dimensional excitable waves govern self-organized morphodynamics of amoeboid cells. *Proc. Natl Acad. Sci. USA* **110**, 5016–5021 (2013).
47. Iglesias, P. A. & Devreotes, P. N. Biased excitable networks: how cells direct motion in response to gradients. *Curr. Opin. Cell Biol.* **24**, 245–253 (2012).
48. Hoeller, O. & Kay, R. R. Chemotaxis in the absence of PIP3 gradients. *Curr. Biol.* **17**, 813–817 (2007).
49. Cai, H. *et al.* Ras-mediated activation of the TORC2-PKB pathway is critical for chemotaxis. *J. Cell Biol.* **190**, 233–245 (2010).
50. Zhang, S., Charest, P. G. & Firtel, R. A. Spatiotemporal regulation of Ras activity provides directional sensing. *Curr. Biol.* **18**, 1587–1593 (2008).
51. Srinivasan, S. *et al.* Rac and Cdc42 play distinct roles in regulating PI(3,4,5)P3 and polarity during neutrophil chemotaxis. *J. Cell Biol.* **160**, 375–385 (2003).
52. Yoo, S. K. *et al.* Differential regulation of protrusion and polarity by PI3K during neutrophil motility in live zebrafish. *Dev. Cell* **18**, 226–236 (2010).
53. Decave, E. *et al.* Shear flow-induced motility of *Dictyostelium discoideum* cells on solid substrate. *J. Cell Sci.* **116**, 4331–4343 (2003).
54. Zhao, M. *et al.* Electrical signals control wound healing through phosphatidylinositol-3-OH kinase-gamma and PTEN. *Nature* **442**, 457–460 (2006).
55. Welf, E. S., Ahmed, S., Johnson, H. E., Melvin, A. T. & Haugh, J. M. Migrating fibroblasts reorient directionality by a metastable, PI3K-dependent mechanism. *J. Cell Biol.* **197**, 105–114 (2012).
56. Westendorf, C. *et al.* Actin cytoskeleton of chemotactic amoebae operates close to the onset of oscillations. *Proc. Natl Acad. Sci. USA* **110**, 3853–3858 (2013).
57. Lee, S., Shen, Z., Robinson, D. N., Briggs, S. & Firtel, R. A. Involvement of the cytoskeleton in controlling leading-edge function during chemotaxis. *Mol. Biol. Cell* **21**, 1810–1824 (2010).
58. Charest, P. G. *et al.* A Ras signaling complex controls the RasC-TORC2 pathway and directed cell migration. *Dev. Cell* **18**, 737–749 (2010).

METHODS

Cells. Wild-type *Dictyostelium discoideum* cells are of the AX2 strain obtained from the Robert Kay laboratory (MRC Laboratory of Molecular Biology, UK). The $g\beta^-$ and $pten^-$ cells were described previously^{59,60}. The parent strains of $g\beta^-$ and $pten^-$ cells were AX3 and AX2, respectively. $plmA^-/piaA^-$ cells were created by deleting $plmA$ in $plmA^-$ cells⁶¹ using homologous recombination. Cells were used within three months of thawing from frozen stocks of the original knockouts. Cells were transformed with plasmids encoding RBD–GFP, PH–RFP, HSPC300–GFP, LimE–RFP, Coroin–GFP or PAK1(GBD)–YFP by electroporation and maintained in HL-5 medium containing G418 ($20\ \mu\text{g ml}^{-1}$) or hygromycin ($50\ \mu\text{g ml}^{-1}$) at 22°C .

Both growth-stage and developed cells were used for microscopy experiments. For most TIRF microscopy, developed cells were used to reduce photosensitivity, which allowed for prolonged and frequent imaging, although cytoskeletal oscillations and waves of the cytoskeletal and signalling markers were also observed in growth-stage cells. Development was also required for cells to respond to cAMP in the excitability experiments (Fig. 2d–h). Cells were developed for 5 h by pulsing with cAMP every 6 min in development buffer (5 mM Na_2HPO_4 , 5 mM KH_2PO_4 , 2 mM MgSO_4 and 0.2 mM CaCl_2). For all other experiments, growth-stage cells were used.

Microscopy. Total internal reflection fluorescence (TIRF) microscopy was carried out with either an Olympus IX71 inverted microscope illuminated by a Kr/Ar laser source or a Nikon Eclipse TiE microscope illuminated by an Ar laser (GFP) and a diode laser (RFP). Images were acquired by a Photometrics Cascade 512B intensified CCD (charge-coupled device) camera controlled by MetaMorph (UCI) or a Photometrics Evolve EMCCD camera controlled by Nikon NIS-Elements. A Dual-View system (Optical Insights, LLC) was used for simultaneous imaging of GFP and RFP fluorescence in doubly labelled cells.

For confocal microscopy to visualize signalling patches in latrunculin- or LY294002-treated cells, a Leica DMI6000 inverted microscope equipped with a Yokogawa CSU10 spinning Nipkow disc with microlenses and illuminated by a Kr/Ar laser was used. Growth-stage cells were transferred to developmental buffer before imaging. Latrunculin A and LY294002 were diluted to the final concentration from a stock solution in DMSO (concentration: 1 mM for latrunculin A and 50 mM for LY294002). Control cells were always treated with an equivalent concentration of DMSO.

t-stacks. The ImageJ (NIH) software was used for image processing and analysis. For t-stacks, TIRF time-lapse videos were opened and converted to greyscale in ImageJ. The ImageJ 3D Viewer plugin was then used to stack the frames from the video. The resampling factor is set to 1 to avoid blurring of activities between frames. To visualize interior activities in Supplementary Fig. 2d–h, a basal level of cellular fluorescence was subtracted from each video before the t-stacks were generated.

Excitability of Ras activation. RBD–GFP was expressed in aca^- cells, which do not produce cAMP on their own. Cells were developed for 5 h by pulsing with cAMP every 6 min in development buffer (5 mM Na_2HPO_4 , 5 mM KH_2PO_4 , 2 mM MgSO_4 and 0.2 mM CaCl_2) and transferred to one-well chamber.

For Fig. 2d, cells in $50\ \mu\text{l}$ buffer were allowed to settle. Stimulations were carried out by mixing an equal volume of buffer containing cAMP to reach the final concentrations ranging from 10^{-10} to 10^{-6} M. The response was calculated from the decrease in the mean cytoplasmic fluorescence from 13 to 20 cells for each stimulus. Cells were washed 3–4 times with buffer and allowed to recover for 5 min before the next stimulus was applied.

For Fig. 2e, cells were stimulated by lowering a micropipette containing $10\ \mu\text{M}$ of cAMP to the viewing field using a FemtoJet microinjector controlled by a micromanipulator (Eppendorf). The compensation pressure of the injection was set at increasingly lower levels to elicit partial responses. Patches both facing towards and away from the micropipette were observed. The mean intensity of the patches on the membrane under low pressure was measured and divided by the mean intensity of fluorescence around the same cell under high-pressure stimulation to obtain the intensity ratio.

For Fig. 2f–h, cells were incubated in $5\ \mu\text{M}$ latrunculin A for 20 min. Stimulation was carried out by lowering a micropipette containing $20\ \mu\text{M}$ of cAMP to the viewing field using a FemtoJet microinjector controlled by a micromanipulator (Eppendorf). For short stimulation, the micropipette was brought to the viewing field for 1 s before lifting, and the total duration of the stimuli is estimated to be 2 s based on the temporal profile of fluorescence from a micropipette filled with Alexa Fluor 594 (not shown). The response was calculated from the decrease in the mean cytoplasmic fluorescence from 7 to 10 cells for each stimulus. For Fig. 2g, the responses were normalized to the peak of the first response. For Fig. 2h, the magnitude of the second responses was fitted to an exponential curve of the form $a - a \cdot 0.5^{(x-c)/t_{1/2}}$ by a nonlinear least-squares method using the program Gnuplot

(<http://www.gnuplot.info/>), which gave the following values: $a = 0.246 \pm 0.012$, $c = 8.8 \pm 1.1$, $t_{1/2} = 7.38 \pm 1.74$ (final parameter \pm asymptotic s.e.m.). In the normalized recovery plot (Fig. 2g), second responses (mean \pm s.d.) for each time point were divided by $a = 0.246$ and then plotted along with the curve $1 - 0.5^{(x-8.8)/7.38}$.

Analysis of signalling and cytoskeletal activities. For measurement of widths of LimE and RBD activities (Fig. 4e,f), the intensity along the cellular boundary was measured. Positions of half-maximal intensity were used to define the boundary of the activities. For expanding regions, the maximal widths were reported.

Patches of activity under confocal microscopy (Fig. 2i) were defined as membrane regions whose intensity was 2 s.d. above the mean cytosolic intensity and which were at least $2\ \mu\text{m}$ in width.

Cell boundary and protrusions. To generate the ‘protrusion’ t-stack (fourth panel in Fig. 4b), a cell boundary video was first generated from the RBD–GFP TIRF video using the ‘Find Edge’ plugin in ImageJ. A frame-shifted cell boundary video was then subtracted from the original video to obtain the protrusions, which were coloured in blue and superimposed on the cell boundary video (in grey). The ‘protrusion’ video was then used to produce the t-stack.

Undulations. To analyse the fluorescence intensity in undulating regions (Fig. 4c), rectangular areas containing oscillatory LimE recruitment were selected from the RBD–GFP and LimE–RFP TIRF videos. The boundary of the cell was defined by the presence of cytoplasmic RBD–GFP. The average intensities of RBD–GFP and LimE–RFP were calculated by the integrated signal divided by the cellular area within the rectangle. The rates of change for RBD, LimE and cellular area (used for correlation coefficient calculations) were defined as the difference between successive frames.

Kymographs. Velocity kymographs in Fig. 4d were obtained by measuring the distance from each pixel in the boundary (defined by the cytoplasmic RBD fluorescence) of the segmented cell in the present frame to the boundary of the segmented cell in the past frame, using the Matlab command bwdist.m. To filter out fast undulations, the comparison was made between segmented shapes using moving averages of 3 (present) and 12 (past) frames. As the perimeter of the cell changed in length over time, successive lines on the kymograph were aligned by minimizing the sum of the Euclidean distances between the coordinates in two successive lines. The RBD and LimE kymographs were obtained by averaging the fluorescence in a small area (approximately 4 pixels wide and 8 pixels into the cell) centred at each boundary pixel and using the same moving average scheme. The distributions of fluorescence intensities (histograms) were based on all pixels that are a distance less than 5 pixels from the edges. Expanding regions were those with positive velocity, with a minimum size of 25 pixels used to filter noise. The non-expanding regions were those along the edge that were not expanding. The correlation between velocity and fluorescence and the difference in fluorescence intensity distributions were robust to changes in the number of frames averaged as well as the sizes of the areas used to filter the data.

Cell migration assay. Wild-type AX2 or $plmA^-/piaA^-$ cells were developed for 5 h with cAMP pulsing every 6 min. Cells were then transferred to 8-well chambers (Lab Tek #155409) at a density of $100\ \text{cells mm}^{-2}$, and treated with $50\ \mu\text{M}$ of LY294002 (Cell Signaling #9901) in 0.1% DMSO or 0.1% DMSO for 1 h. Migration videos were recorded at 1 min intervals for 1 h.

Chemorepellent experiments. For LY294002 repellent experiments (Fig. 6c–e), a micropipette filled with $200\ \mu\text{M}$ LY294002 in 0.4% DMSO or 0.4% DMSO alone was introduced into a field of growth-stage *Dictyostelium* cells at 0 min. Migration videos were recorded at 1 min intervals for 20 min. The chemotaxis index is defined as the cosine of the angle between the direction of movement and the direction from the start point to the micropipette.

Statistical analysis and repeatability of experiments. Statistical significance and P values were determined using the two-tailed Student’s t-test. One-way analysis of variance was used to compare the four groups in Fig. 2i. Mean values \pm either s.d. or s.e.m. were reported as indicated in the figure legends except for Fig. 4e, in which a box plot was used to show the minimums, maximums and quartiles of the distribution.

Two independent experiments were performed for Figs 1d, 2d,e,g–j, 3b,d, 4c and 6e; three independent experiments for Figs 1e,g, 2c,f and 4e,f; and six independent experiments for Fig. 1c. Statistics were derived by aggregating the n numbers noted in each figure legend across independent experiments.

Representative images associated with Figs 1d,e,g, 2e and 6e are shown along with statistics. Representative images Fig. 1a,b are associated with Fig. 1c and Fig. 3a,c associated with Fig. 3b; and Fig. 4a,b are associated with Fig. 4c.

Representative images are also used for Figs 1f, 2a,b and 6b, which have been routinely observed in the laboratory (in more than 3 independent experiments). Fig. 6a,c shows representative results of 3 independent experiments.

Computer simulation of coupled systems. Here we describe the mathematical model of the coupled networks. The model consists of two coupled reaction–diffusion systems: a slow excitable system, reflecting the behaviour of the signal transduction excitable network (STEN), similar to the system introduced previously^{24,47}; and a fast oscillatory system, reflecting the behaviour of the cytoskeletal oscillatory network (CON).

Previously we suggested that the signalling network can be described by an excitable system whose activity is biased by the external receptor signal²⁴. This was illustrated by an activator–inhibitor system that is qualitatively similar to the FitzHugh–Nagumo model for action potentials, which is itself a simplification of the Hodgkin–Huxley model of action potentials⁶².

The system is described by two species (Supplementary Fig. 4a). Component X_s acts as the activator: it is autocatalytic (it has strong positive feedback), and also activates the downstream component—we refer to this as the feedforward loop. The Y_s component provides negative feedback to X_s . The evolution of the activities of these two species is described by a reaction–diffusion system, consisting of the following partial differential equations:

$$\begin{aligned}\frac{\partial X_s}{\partial t} &= \alpha_s \frac{X_s^2}{k_s^2 + X_s^2} - \beta_s X_s - \gamma_s Y_s + U_s + D_{X_s} \nabla^2 X_s \\ \frac{\partial Y_s}{\partial t} &= \delta_s X_s - \varepsilon_s Y_s + D_{Y_s} \nabla^2 Y_s\end{aligned}$$

Both components in this system can diffuse spatially, with diffusion coefficients D_{X_s} and D_{Y_s} , respectively. The coefficients $\alpha_s, \beta_s, \gamma_s, \delta_s, \varepsilon_s$ and k_s are constants. The signal U_s is the input to the slow system, which consists of two components: a basal level of activation (B_s) and the contribution from the fast system ($f(X_f)$, described below):

$$U_s = B_s + f(X_f)$$

Note that in contrast to the biased-excitatory network described previously²⁴, here we do not incorporate the contribution of receptor signalling. Were this to be included, it would be as an additional term in U_s . We also do not incorporate a stochastic component directly into the slow system, but instead achieve this through the faster system. However, such a stochastic component could explain the signalling patches observed in latrunculin-treated cells (Fig. 2a,b).

In the absence of a triggering from the fast system, the slow system has a single steady state that is stable (Supplementary Fig. 4a,b). Small, sub-threshold disturbances to this steady state do not trigger the excitable behaviour of the system. However, if the perturbation is above a threshold, a large excursion in the phase plane takes place before the system settles back to the equilibrium.

To describe the behaviour of the CON, we use a stochastic, bi-stable oscillator involving an activator (X_f) and an inhibitor (Y_f). The form of the equations is identical:

$$\frac{\partial X_f}{\partial t} = \alpha_f \frac{X_f^2}{k_f^2 + X_f^2} - \beta_f X_f - \gamma_f Y_f + U_f + D_{X_f} \nabla^2 X_f \quad (1)$$

$$\frac{\partial Y_f}{\partial t} = \delta_f X_f - \varepsilon_f Y_f + D_{Y_f} \nabla^2 Y_f \quad (2)$$

The input to this system (U_f) consists of three parts:

$$U_f = B_f + N_f + g(X_s)$$

As above, B_f represents the basal level of activation and $g(X_s)$ the contribution of the slow system to the fast system (described in detail below). This system also includes a component that incorporates stochastic fluctuations (N_f). These fluctuations are modelled as a zero mean, unit variance white noise process.

Systems involving cubic nullclines such as those described by Equations (1) and (2) can be oscillatory, as in the popular relay oscillator. In our system, however, we chose the coefficients $\alpha_f, \beta_f, \gamma_f, \delta_f, \varepsilon_f$ and k_f so that, in the absence of noise or a contribution from the slow network ($N_f = 0, g(X_s) = 0$), the system has three steady states, two of which are stable and the other unstable (Supplementary Fig. 4c,d). These two stable steady states are such that small, but superthreshold perturbations, make the system switch from one equilibrium to the other, resulting in oscillatory-like behaviour. In this case, noise endows the system with oscillatory behaviour. Similar behaviour has been documented previously^{63–65}.

The two systems are coupled in a bidirectional manner. However, because the only external input to the coupled systems is through the external stochastic

component of the fast system, perturbations from the respective equilibria have to be initiated through the fast system.

The function $f(X_f)$ is used as a trigger to the slow system based on the activity of the fast system. First, at each angle $\theta_0 \in (-\pi, \pi]$ along the perimeter of the cell, the activity of the fast system in the neighbourhood of θ_0 is summed:

$$\tilde{X}_f(\theta_0) = \int_{\theta_0 - \Delta\theta}^{\theta_0 + \Delta\theta} X_f(\theta) d\theta$$

We used a width of $\Delta\theta = 15^\circ$. This is used to generate a switch-like function:

$$h(X_f(\theta)) = \begin{cases} 0, & \text{if } \tilde{X}_f(\theta) < \tilde{X}_{f-th} \\ 1, & \text{otherwise} \end{cases}$$

The coupling term $f(X_f)$ is obtained by multiplying this function by a white-noise component:

$$f(X_f(\theta)) = h(X_f(\theta)) \tilde{N}_f$$

which represents a probabilistic component of the activation. Here \tilde{N}_f is a white-noise process with unit variance and a mean of 0.05.

After the slow system is triggered, the high activity of X_s starts to regulate and synchronize the fast system. During the time that the slow system fires up, high input from $g(X_s)$ will drive the fast system into a higher stable steady state. After $g(X_s)$ vanishes, the fast system resumes an oscillatory mode. The function of $g(X_s)$ is simply described with an ‘on–off’ switch function:

$$g(X_s(\theta)) = \begin{cases} g_B, & \text{if } X_s(\theta) < X_{s-th} \\ g_s, & \text{otherwise} \end{cases}$$

The model includes a number of parameters. Our starting point for choosing these was the previous model of the biased excitable network²⁴. However, we adjusted these parameters so that the activity of the slow system spreads out to about 50 degrees around the perimeter and that the activities last about 100 s, to match the observed experimental behaviour of the STEN. These changes were made by reducing the parameters that dictate the speed of the system and by altering the relative contribution of the two diffusion coefficients. For the fast system we chose the parameters so that the system had two stable equilibria (by changing the slope of the Y_f nullcline). We also adjusted the speed of the system so that the oscillations lasted about ten seconds. This is accomplished by adjusting the level of the noise. The final parameter values are given in Supplementary Table 1.

The model and all simulations are implemented using Matlab (MathWorks). The computer code is available on request. The cell was represented as a one-dimensional system using periodic boundaries. The cell boundary was discretized using 360 points.

Spatial diffusion terms, which contain the second derivatives, are approximated by central differences in space (in one dimension); and by doing that, the partial differential equations are converted to ordinary differential equations. The solution of the stochastic differential equations was obtained using the free SDE toolbox for Matlab: (<http://sdetoolbox.sourceforge.net>). The time step for the simulation is set to 0.025 s.

To determine the effect of the model activities on the shape of a cell we used a level set framework to simulate cell shape changes as previously described^{66,67}.

In short, in the level set method the cell is described as the zero-level set of a potential function $\varphi(x,t)$, $x \in \mathbf{R}^2$. The evolution of the cell is described by the Hamilton–Jacobi equation

$$\frac{\partial \varphi(x,t)}{\partial t} = v(x,t) \cdot \nabla \varphi(x,t) = 0 \quad (3)$$

where the $v(x,t)$ describes the local velocity of the potential function. To obtain this velocity we apply different stresses on the cell and use a viscoelastic mechanical model of the cell to determine the local velocity. In our case we use:

$$\dot{x}_m = -(K/D)x_{cor} + (1/D + 1/B)\sigma_{tot}$$

$$\dot{x}_{cor} = -(K/D)x_{cor} + (1/D)\sigma_{tot}$$

where σ_{tot} is the total stress applied on the cell, x_m and x_{cor} are the local displacements of the membrane and cortex, respectively, and K , D and B are viscoelastic components of the cell describing the elasticity (K) and viscosity (D) of the membrane, and the viscosity of the (B) of the cytoplasm. The velocity in equation (3) is given by $v = \dot{x}_m$.

The total net stress (σ_{tot}) includes the vector sum of the stresses acting on the cell. This stress includes contributions from passive components, such as surface tension (σ_{ten}) as well as protrusive forces (σ_{pro}) driven by the fast oscillatory network. Unlike previous simulations^{66,67}, we do not impose area constraints on the cell, as these simulations are of cells being observed using TIRF microscopy. The component due to surface tension is given by

$$\sigma_{\text{ten}} = \gamma \kappa(x) \mathbf{n}$$

where γ is the local cortical tension, κ is the local curvature and \mathbf{n} is a normal unit vector.

The protrusive stresses are proportional to the fast oscillatory signal Y_f :

$$\sigma_{\text{pro}} = \sigma_0 Y_f(\theta) \mathbf{n}$$

Parameters used in these simulations are provided in Supplementary Table 1. This model was implemented using the Level Set Toolbox for Matlab⁶⁸.

59. Wu, L., Valkema, R., Van Haastert, P.J. & Devreotes, P. N. The G protein beta subunit is essential for multiple responses to chemoattractants in *Dictyostelium*. *J. Cell Biol.* **129**, 1667–1675 (1995).

60. Iijima, M. & Devreotes, P. Tumor suppressor PTEN mediates sensing of chemoattractant gradients. *Cell* **109**, 599–610 (2002).
61. Chen, L. *et al.* PLA2 and PI3K/PTEN pathways act in parallel to mediate chemotaxis. *Dev. Cell* **12**, 603–614 (2007).
62. Fitzhugh, R. Impulses and physiological states in theoretical models of nerve membrane. *Biophys. J.* **1**, 445–466 (1961).
63. Kim, J., Heslop-Harrison, P., Postlethwaite, I. & Bates, D. G. Stochastic noise and synchronisation during *Dictyostelium* aggregation make cAMP oscillations robust. *PLoS Comput. Biol.* **3**, e218 (2007).
64. Vilar, J. M., Sole, R. V. & Rubi, J. M. Noise and periodic modulations in neural excitable media. *Phys. Rev. E* **59**, 5920–5927 (1999).
65. Weinberger, L. S., Burnett, J. C., Toettcher, J. E., Arkin, A. P. & Schaffer, D. V. Stochastic gene expression in a lentiviral positive-feedback loop: HIV-1 Tat fluctuations drive phenotypic diversity. *Cell* **122**, 169–182 (2005).
66. Yang, L. *et al.* Modeling cellular deformations using the level set formalism. *BMC Syst. Biol.* **2**, 68 (2008).
67. Poirier, C. C., Ng, W. P., Robinson, D. N. & Iglesias, P. A. Deconvolution of the cellular force-generating subsystems that govern cytokinesis furrow ingression. *PLoS Comput. Biol.* **8**, e1002467 (2012).
68. Mitchell, I. M. The flexible, extensible and efficient toolbox of level set methods. *J. Sci. Comput.* **35**, 300–329 (2008).

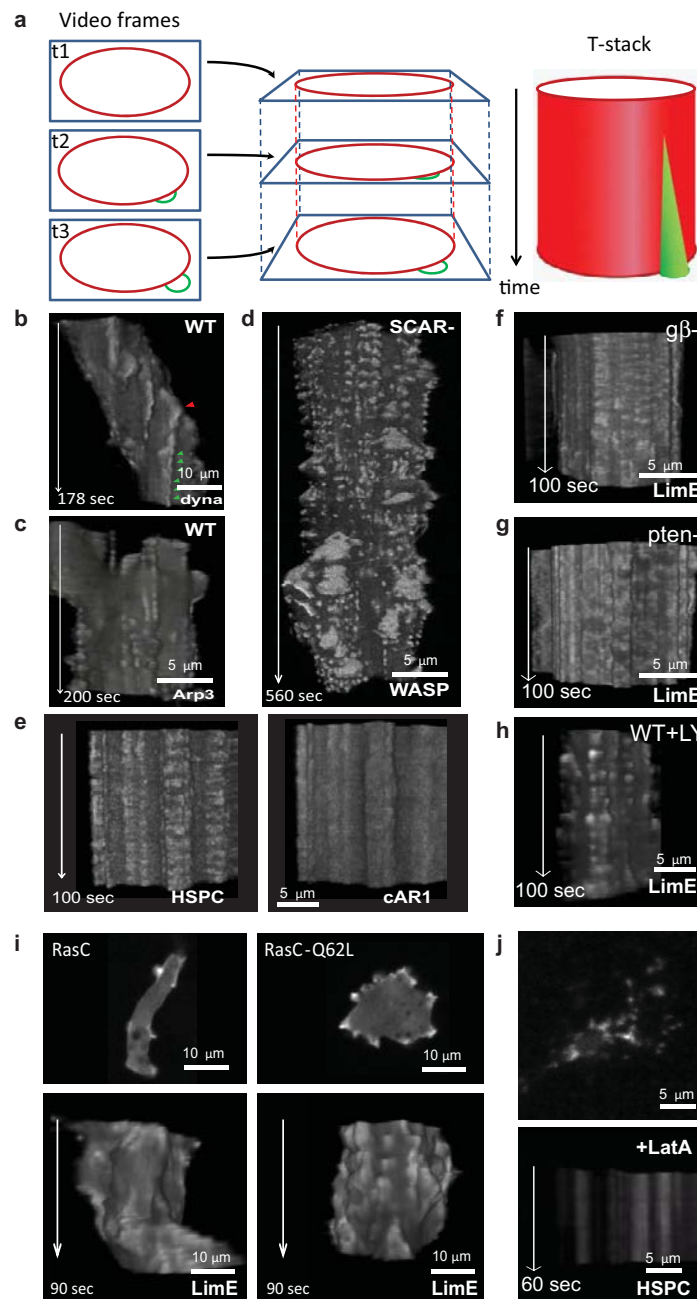


Figure S1 Cytoskeletal network. (a) Illustration of the t-stack technique. The frames of a TIRF video (left) are stacked to produce the t-stack (right). The position and orientation of frames t1, t2, and t3 in the t-stack is shown (middle). The immobile red oval generates the red cylinder in the t-stack, while the expansion of the green region over time creates the oblique cone-like appendage. (b-d) T-stacks derived from published TIRF time-lapse videos of a wild-type cell expressing GFP-dynactin (b)¹, a wild-type cell expressing GFP-Arp3 (c)², and a SCAR- cell expressing GFP-WASP (d)³ showing fast oscillations of cytoskeletal proteins. The red arrowhead

indicates a pseudopodium preceding oscillations of dynactin (green arrowheads). (e) T-stacks from a cell co-expressing HSPC300-GFP and cAR1-RFP. (f-h) T-stacks of LimE expressed in $g\beta^-$ cells (f), *pten*- cells (g), and LY294002-treated wild-type cells (h). (i) Cytoskeletal oscillations in cells expressing constitutively active Ras. LimE-RFP in *rasC*- cells expressing Flag-RasC (left) or Flag-RasCQ62L (right). The videos used for these t-stacks were published earlier⁴. (j) TIRF image (top) and t-stack (bottom) of a latrunculin-treated cell expressing HSPC300-GFP, showing foci of fluorescence that did not oscillate.

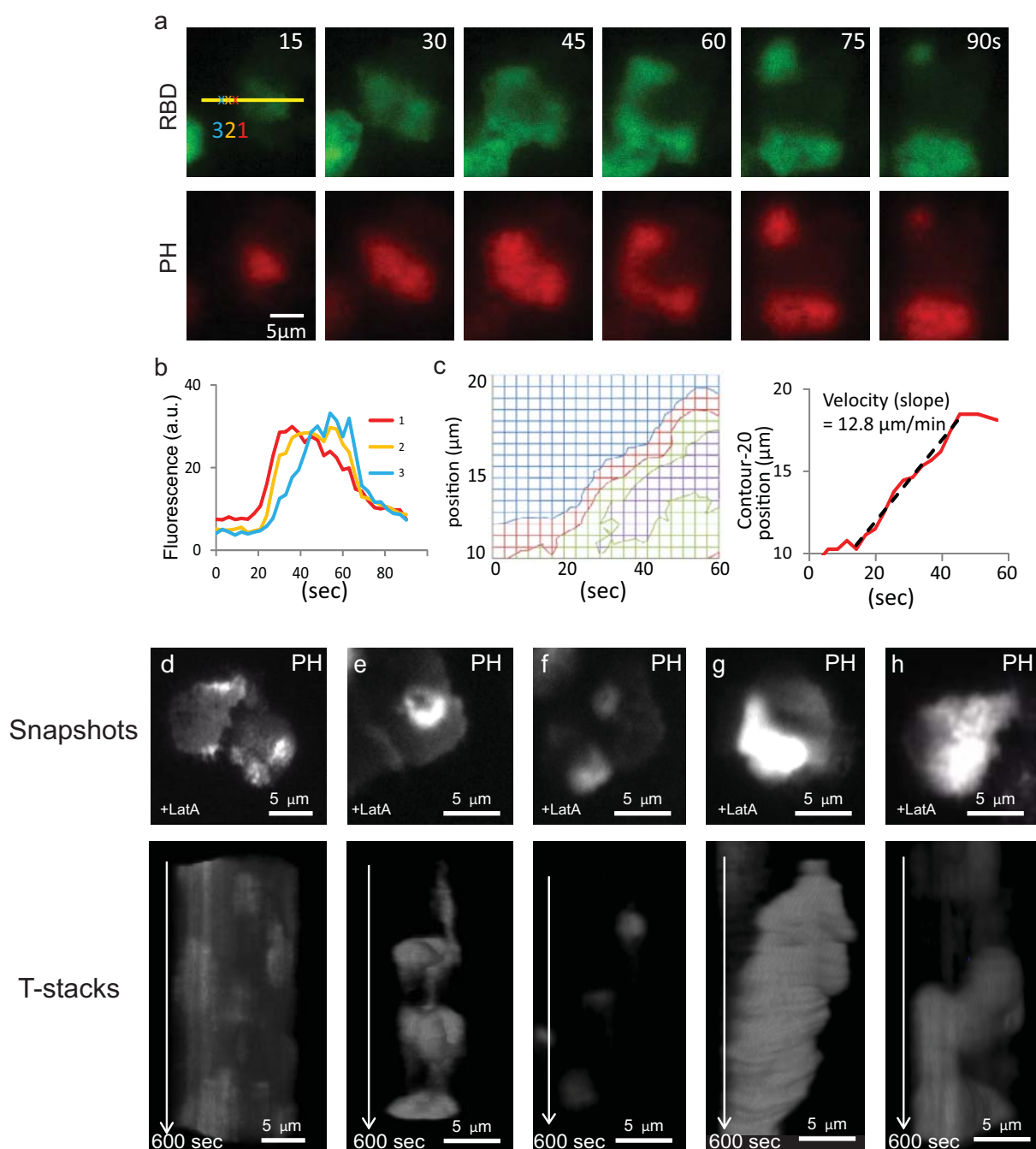


Figure S2 Signal transduction network. (a) TIRF images of a cell co-expressing RBD-GFP and PH-RFP showing coordinated propagation of RBD and PH waves. Video rate was 3 spf (Supplementary Movie S3). (b) The temporal profiles of RBD intensity at three spots marked 1, 2, 3 in (a). (c) The progression of contour lines for gray values 10, 20 and 30 along the yellow line in (a) was used to calculate the speed of the wave propagation. In the example, the speed of the wave between 15 sec and 48 sec was

12.8 $\mu\text{m}/\text{min}$ by fitting the gray value 20 contour with a least square line. (d-h) Snapshots from TIRF videos of PH-GFP in cells treated with 4 μM latrunculin A (top, Supplementary Movies S4-S8) and the corresponding t-stacks (bottom). Panels (e) and (f) are the same cells at different times, (h) is the same cell as the left cell in (d), and (g) is a different cell. To visualize interior activities, a basal level of cellular fluorescence was subtracted from each video before the t-stacks were generated.

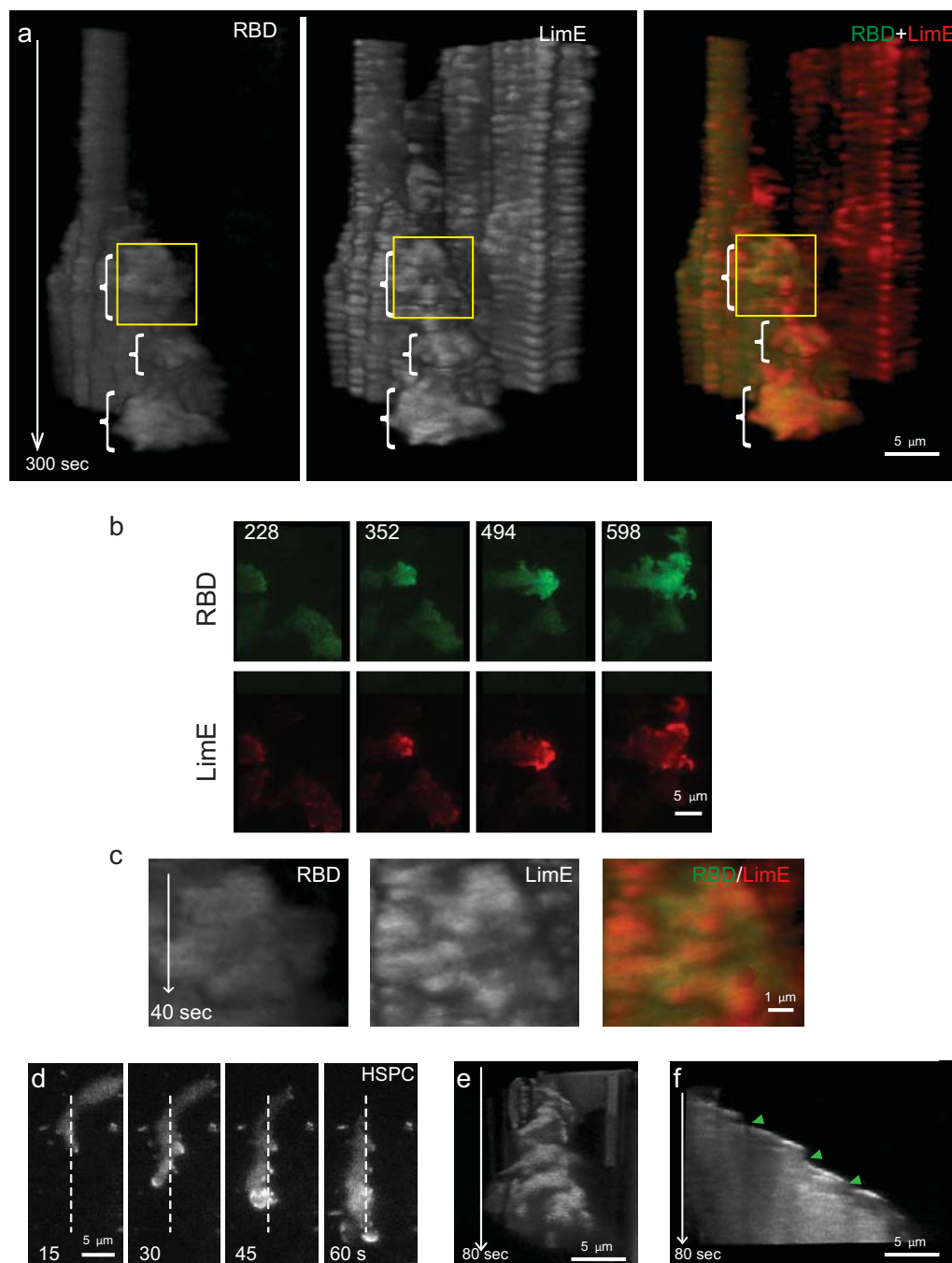


Figure S3 Signaling and cytoskeletal activities on protrusions. (a) T-stacks of two cells co-expressing RBD-GFP and LimE-RFP as well as the merged t-stack. The brackets in the cell on the left point to protrusions with high RBD and LimE. The cell on the right has very low level of RBD-GFP expression, but fast LimE oscillations are visible. Note that weak oscillations in the RBD t-stack (left cell) reflect changes in the boundary which delineates cytosolic RBD rather than RBD intensity on the cortex. Video rate was 2 spf. (b) Frames from a TIRF

video of cells co-expressing RBD-GFP and LimE-RFP showing the distributions of RBD and LimE in protrusions. (c) Close-up views of a protrusion (yellow boxes in (a)) showing a smoother change of RBD intensity compared with that of LimE. (d) Frames from the TIRF video of a single large protrusion of a cell expressing HSPC300-GFP (Supplementary Movie S10). (e) t-stack of the video in (d). (f) Kymograph across the dashed line in (d). Arrowheads point to pauses in HSPC300 recruitment where cell boundary expansion stalled.

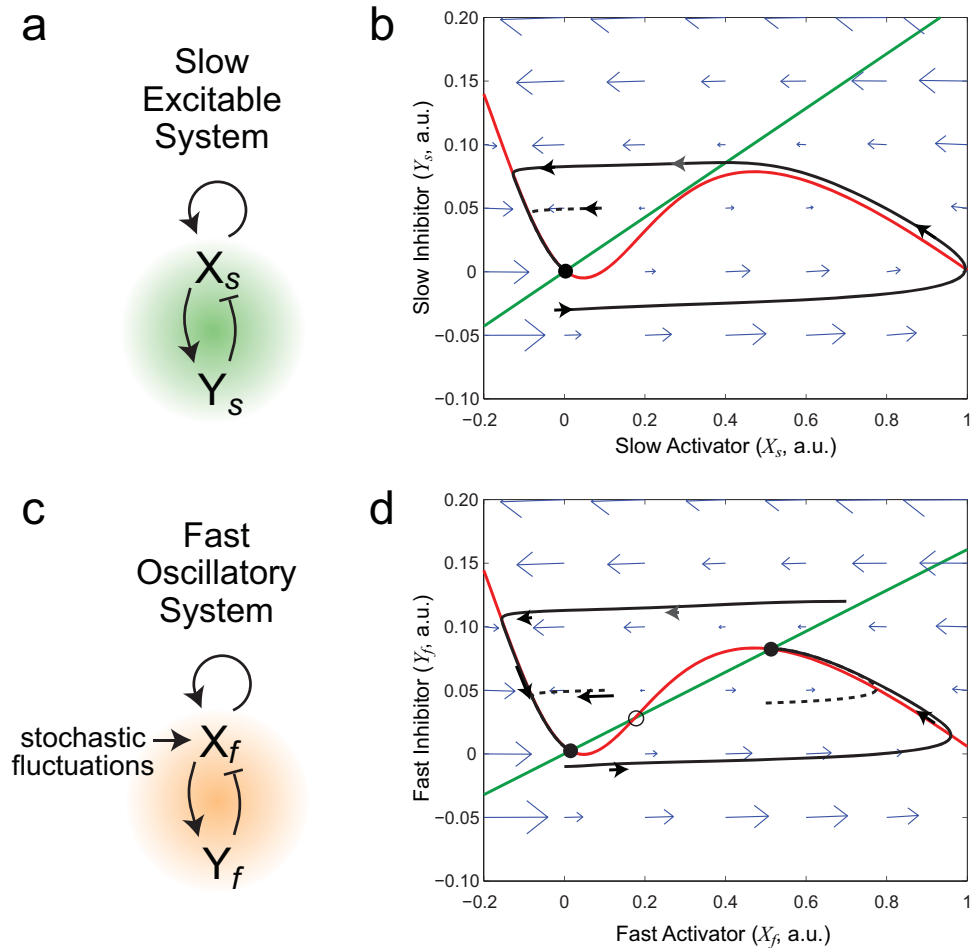


Figure S4 Simulation of coupled systems. (a) The slow excitable system is implemented as an activator (X_s)-inhibitor (Y_s) system. (b) Phase plane plot of the slow excitable system. Red and green lines are nullclines for the activator and inhibitor components, respectively. The solid black circle represents the unique, stable equilibrium, found at the intersection of the two nullclines. The blue arrows represent the system evolution at different points in the phase plane. Two different trajectories are denoted by the black lines. The dotted black line represents a sub-threshold perturbation from which the system returns quickly to the equilibrium. The solid black line illustrates a super-threshold perturbation that causes the system to

undergo a large excursion before returning to the equilibrium. (c) The Fast oscillatory system is also implemented using an activator (X_f)-inhibitor (Y_f) system and also incorporates the influence of stochastic perturbations. (d) Phase plane plot of the fast oscillatory system. Red and green lines are nullclines for the activator and inhibitor components, respectively. In this case the system has three equilibria, at the points where the nullclines intersect. The solid black circles denote two stable equilibria, the open black circle the unique, unstable equilibrium. The blue arrows represent the evolution at different points in the phase plane. Trajectories are denoted by the black lines.

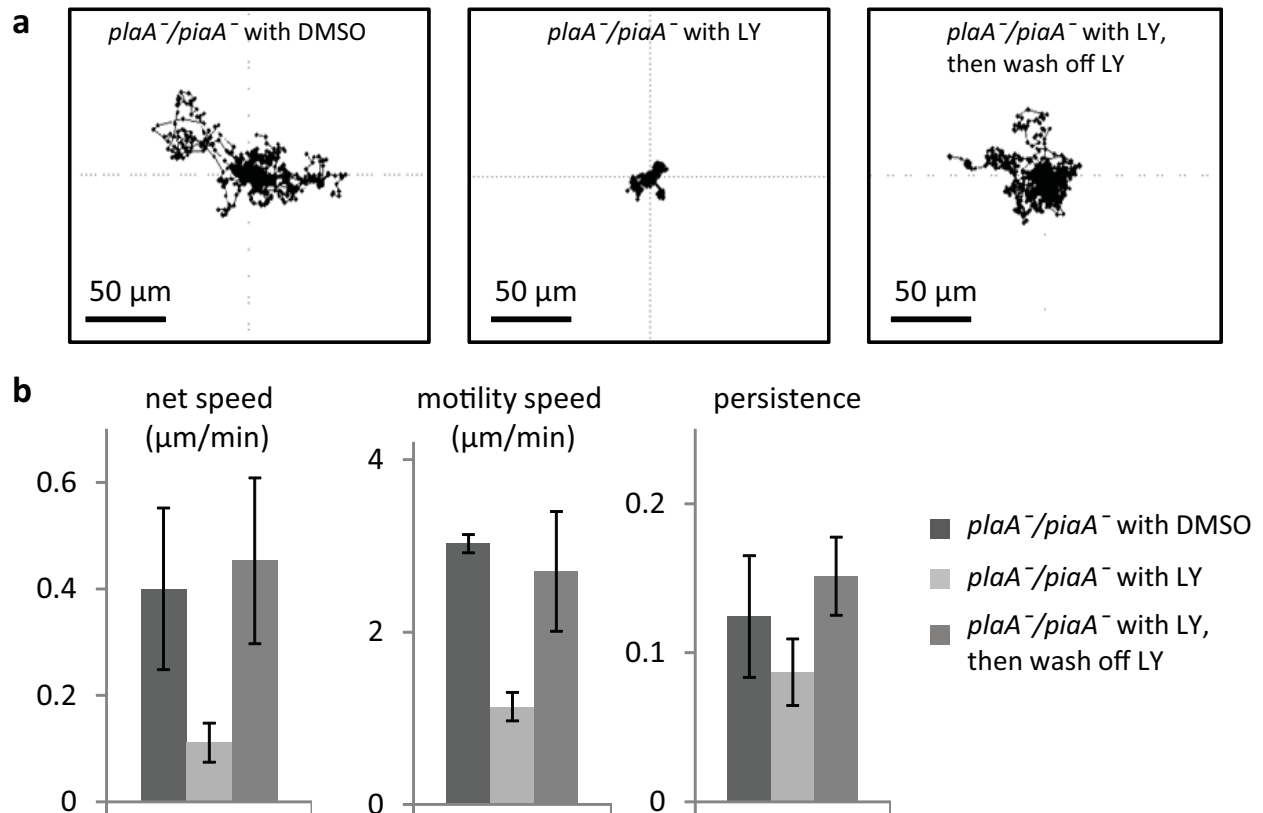


Figure S5 Washout of LY294002 reversed the motility to *plaA⁻/piaA⁻* cells. (a) Trajectories of cell migration. Random migration of cells were recorded and quantified as in Figure 6. For the LY washout experiment, cells were changed to buffer without LY294002, and allowed to settle for 40 min before

recording was started. Duration of tracks is 60 min. (b) Quantification of net speed, motility speed, and persistence (mean ± S.D. from n=4, 3, 3 experiments for *plaA⁻/piaA⁻* with DMSO, *plaA⁻/piaA⁻* with LY294002, and wash off, respectively. The source data is provided in Table S2.)

Supplementary Table

Table S1. Parameter values for simulations.

Slow Network		Fast Network		Coupling	
D_{x_s}	0.0059 $\mu\text{m}^2/\text{s}$	D_{x_f}	0.091 $\mu\text{m}^2/\text{s}$	$X_{f\text{-th}}$	7 A.U.
D_{y_s}	0.0151 $\mu\text{m}^2/\text{s}$	D_{y_f}	0.0236 $\mu\text{m}^2/\text{s}$	$X_{s\text{-th}}$	0 A.U.
α_s	0.7 s^{-1}	α_f	0.19 s^{-1}	g_B	1.25 A.U.
β_s	0.63 s^{-1}	β_f	0.18 s^{-1}	g_s	1.3 A.U.
γ_s	2.35 s^{-1}	γ_f	0.65 s^{-1}		
δ_s	$5.1 \times 10^{-3} \text{ s}^{-1}$	δ_f	$1.1 \times 10^{-3} \text{ s}^{-1}$		
ε_s	$2.4 \times 10^{-2} \text{ s}^{-1}$	ε_f	$6.7 \times 10^{-3} \text{ s}^{-1}$		
k_s	0.32 A.U.	k_f	0.32 A.U.		
B_s	-0.0138 A.U.	B_f	0.1 A.U.		
Viscoelastic Parameters					
K	0.098 nN/ μm^3	D	0.064 nN-s/ μm^3	B	6.09 nN-s/ μm^3
γ	1 nN/ μm	σ_0	35 nN/ μm^2		

Table S2. Statistics source data

Fig. S5b statistics

Treatment	Experiment #	motility speed		persistence	net speed
PlaA-/Pia- with DMSO	1	2.947		0.12	0.397
PlaA-/Pia- with DMSO	2	2.959		0.067	0.236
PlaA-/Pia- with DMSO	3	2.964		0.091	0.245
PlaA-/Pia- with DMSO	4	3.168		0.162	0.558
	Average	3.0263333		0.1243333	0.4
	STDEV	0.1059072		0.0408819	0.1518442
PlaA-/Pia- with LY	1	1.042		0.067	0.085
PlaA-/Pia- with LY	2	1.036		0.083	0.096
PlaA-/Pia- with LY	3	1.326		0.111	0.153
	Average	1.1346667		0.087	0.1113333
	STDEV	0.1657267		0.0222711	0.0365011
PlaA-/Pia- with LY then wash off	1	2.137		0.127	0.333
PlaA-/Pia- with LY then wash off	2	3.479		0.179	0.629
PlaA-/Pia- with LY then wash off	3	2.501		0.148	0.396
	Average	2.7056667		0.1513333	0.4526667
	STDEV	0.6940154		0.0261598	0.1559241

Supplementary Video Legends

Video S1 HSPC300-GFP. Time-lapse TIRF video of a *Dictyostelium* cell expressing HSPC300-GFP with a rate of 1 spf. The video is shown at 15 frames/s and corresponds to Fig. 1a, b.

Video S2 T-stack of HSPC300-GFP. Rotation of the t-stack along its t(time)-axis. The speed of the rotation is shown at 40 degrees/s. The t-stack was generated from Movie S1 and corresponds to Fig. 1b.

Video S3 RBD-GFP and PH-RFP. Time-lapse TIRF video of a *Dictyostelium* cell expressing RBD-GFP and PH-RFP with a rate of 3 spf. The video is shown at 15 frames/s and corresponds to Fig. S2a.

Video S4 PH-GFP in latrunculin-treated cell. Time-lapse TIRF video of latrunculin-treated *Dictyostelium* cells expressing PH-GFP with a rate of 5 spf. The video is shown at 15 frames/s and corresponds to Supplementary Fig. S2d.

Video S5 PH-GFP in latrunculin-treated cell. Time-lapse TIRF video of latrunculin-treated *Dictyostelium* cells expressing PH-GFP with a rate of 5 spf. The video is shown at 15 frames/s and corresponds to Supplementary Fig. S2e.

Video S6 PH-GFP in latrunculin-treated cell. Time-lapse TIRF video of latrunculin-treated *Dictyostelium* cells expressing PH-GFP with a rate of 10 spf. The video is shown at 15 frames/s and corresponds to Supplementary Fig. S2f.

Video S7 PH-GFP in latrunculin-treated cell. Time-lapse TIRF video of a latrunculin-treated *Dictyostelium* cell expressing PH-GFP with a rate of 10 spf. The video is shown at 15 frames/s and corresponds to Supplementary Fig. S2g.

Video S8 PH-GFP in latrunculin-treated cell. Time-lapse TIRF video of latrunculin-treated *Dictyostelium* cells expressing PH-GFP with a rate of 10 spf. The video is shown at 15 frames/s and corresponds to Supplementary Fig. S2h.

Video S9 RBD-GFP and LimE-RFP in undulations and protrusions. Time-lapse TIRF video of a *Dictyostelium* cell co-expressing RBD-GFP and LimE-RFP with a rate of 2 spf. Cytoplasmic fluorescence of RBD-GFP and LimE-RFP was subtracted to highlight areas of increased intensity. Cell boundary (in gray) was derived from the cytoplasmic fluorescence of RBD-GFP. The video is shown at 7 frames/s and corresponds to Fig. 4b.

Video S10 HSPC300-GFP in protrusion. Time-lapse TIRF video of a *Dictyostelium* cell expressing HSPC300-GFP with a rate of 1 spf. The video is shown at 15 frames/s and corresponds to Supplementary Fig. S3d-f.

Video S11 Computer simulation of the STEN-CON coupling model. Level set simulation of cell movement along with the activities of the slow (Ys, in green) and fast (Yf, in red) systems as well as the merged activities. Cell membrane is driven by the signal of Yf (see Extended Experimental Procedures for simulation details). The video is shown at 20 frames/s.

Supplementary References

1. Kabacoff, C. *et al.* Dynacortin facilitates polarization of chemotaxing cells. *BMC Biol* 5, 53 (2007).
2. Bretschneider, T. *et al.* Dynamic actin patterns and Arp2/3 assembly at the substrate-attached surface of motile cells. *Curr Biol* 14, 1-10 (2004).
3. Veltman, D.M., King, J.S., Machesky, L.M. & Insall, R.H. SCAR knockouts in *Dictyostelium*: WASP assumes SCAR's position and upstream regulators in pseudopods. *J Cell Biol* 198, 501-508 (2012).
4. Cai, H. *et al.* Ras-mediated activation of the TORC2-PKB pathway is critical for chemotaxis. *J Cell Biol* 190, 233-245 (2010).